iScience

CellPress
OPEN ACCESS

Article

A multi-tissue multi-omics analysis reveals distinct kineztics in entrainment of diurnal transcriptomes by inverted feeding

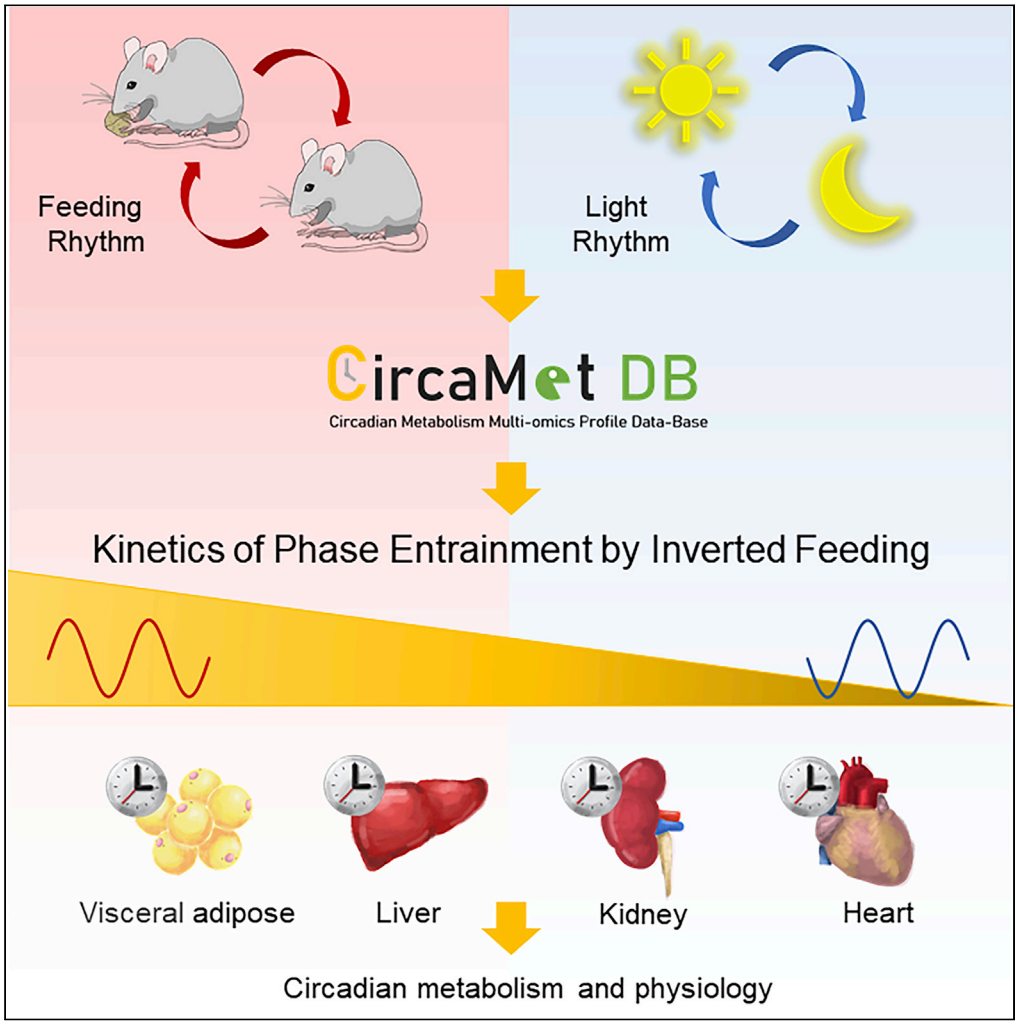

Haoran Xin, Fang Deng, Meiyu Zhou, ..., Guanghou Shui, Zhihui Zhang, Min-Dian Li

xyzpj@tmmu.edu.cn (Z.Z.)
mindianli@tmmu.edu.cn (M.-D.L.)

Highlights

A multi-omics analysis of food entrainment in mouse peripheral tissues

Inverted feeding rhythm entrains diurnal transcriptomes with distinct kinetics

Phase kinetics of tissue clocks is conditioned by constant light

Cardiac metabolism entrains to feeding fast with slow kinetics of the heart clock

Xin et al., iScience 24, 102335
April 23, 2021
https://doi.org/10.1016/j.isci.2021.102335

iScience

CellPress
OPEN ACCESS

Article

A multi-tissue multi-omics analysis reveals distinct kineztics in entrainment of diurnal transcriptomes by inverted feeding

Haoran Xin,[1,4] Fang Deng,[2,4] Meiyu Zhou,[1] Rongfeng Huang,[1] Xiaogen Ma,[1] He Tian,[3] Yan Tan,[2] Xinghua Chen,[1] Dan Deng,[1] Guanghou Shui,[3] Zhihui Zhang,[1,*] and Min-Dian Li[1,5,*]

SUMMARY

Time of eating synchronizes circadian rhythms of metabolism and physiology. Inverted feeding can uncouple peripheral circadian clocks from the central clock located in the suprachiasmatic nucleus. However, system-wide changes of circadian metabolism and physiology entrained to inverted feeding in peripheral tissues remain largely unexplored. Here, we performed a 24-h global profiling of transcripts and metabolites in mouse peripheral tissues to study the transition kinetics during inverted feeding, and revealed distinct kinetics in phase entrainment of diurnal transcriptomes by inverted feeding, which graded from fat tissue (near-completely entrained), liver, kidney, to heart. Phase kinetics of tissue clocks tracked with those of transcriptomes and were gated by light-related cues. Integrated analysis of transcripts and metabolites demonstrated that fatty acid oxidation entrained completely to inverted feeding in heart despite the slow kinetics/resistance of the heart clock to entrainment by feeding. This multi-omics resource defines circadian signatures of inverted feeding in peripheral tissues (www.CircaMetDB.org.cn).

INTRODUCTION

Diurnal oscillations of metabolism, physiology, and behavior is pervasive in life, serving to align the body with environmental cycles and to separate chemically incompatible biochemical reactions (Bass and Lazar, 2016; Takahashi, 2017). Circadian clock enables circadian rhythms of metabolism and physiology in cells, which is reset by daily cycles of two principal environmental cues, such as light and food (Kinouchi and Sassone-Corsi, 2020). Although each cell shares a remarkably similar set of clock genes, tissue clocks are organized in a network and paced by the suprachiasmatic nucleus of the hypothalamus (Dibner et al., 2010; Greco and Sassone–Corsi, 2019). The SCN clock entrains to the light-dark cycle and synchronizes clocks in peripheral tissues, including liver, kidney, heart, and fat tissue, in part through feeding behaviors (Schibler et al., 2016). It is thought that food overrides light in resetting most, if not all, peripheral clocks (Reinke and Asher, 2019). Inverted feeding, also known as daytime-restricted feeding (DRF) or desynchronized feeding, entrains the liver clock to completely inverted oscillations in rodents under light/dark cycles (Damiola et al., 2000; Stokkan et al., 2001).

The coupling between peripheral clocks and feeding rhythms is conducted by nutrient-sensing signaling (Crosby et al., 2019; Hirano et al., 2016; Panda, 2016; Reinke and Asher, 2019; Zhang et al., 2020b). Molecular gears of circadian clocks are primarily made of transcriptional-translational feedback loops, including transcription factors BMAL1, CLOCK, and corepressors PERIOD (PER) and CRY (Patke et al., 2020; Takahashi, 2017). Poly(ADP-ribose) polymerase 1 senses intracellular level of NAD+ and entrains the liver clock to inverted feeding via ploy(ADP-ribosyl)ation of CLOCK (Asher et al., 2010). Glucose-sensing OGT O-GlcNAcylates clock proteins (Yang and Qian, 2017) and modulates diurnal rhythms of voluntary locomotion (Kaasik et al., 2013) and glucose homeostasis (Li et al., 2013). In the past, although many studies focused on clock entrainment in liver, it is not clear whether the regulatory mechanisms of the liver clock are applicable to other peripheral tissues. Emerging evidence suggested that entrainment of peripheral clocks is conditioned by light and non-cell autonomous clocks. The functioning of the liver clock requires the presence of BMAL1-dependent clocks in other tissues under constant darkness (Koronowski et al., 2019), which applies to the epidermal clock (Welz et al., 2019).

[1]Department of Cardiology and the Center for Circadian Metabolism and Cardiovascular Disease, Southwest Hospital, Third Military Medical University (Army Medical University), Chongqing, 400038, China

[2]Department of Pathophysiology, College of High Altitude Military Medicine, Third Military Medical University (Army Medical University), Chongqing, 400038, China

[3]State Key Laboratory of Molecular Developmental Biology, Institute of Genetics and Developmental Biology, Chinese Academy of Sciences, Beijing, 100101, China

[4]These authors contributed equally

[5]Lead contact

*Correspondence: xyzpj@tmmu.edu.cn (Z.Z.), mindianli@tmmu.edu.cn (M.-D.L.)

https://doi.org/10.1016/j.isci.2021.102335

Time-restricted feeding (tRF, also known as nighttime-restricted feeding, NRF) is arising as an effective measure to synchronize diurnal oscillations of physiology and metabolism (Longo and Panda, 2016). In liver, circadian clocks control diurnal rhythms of transcriptomes and metabolomes under constant darkness (Krishnaiah et al., 2017; Vollmers et al., 2009). Hepatocyte-autonomous clock contributes to only 20% of diurnal transcriptomes in liver and is sufficient to establish circadian rhythms of glycogen turnover and NAD + salvage metabolism (Koronowski et al., 2019). However, synchronized feed-fast cycles by tRF restores the majority of diurnal transcriptomes in Bmal1$^{-/-}$ mouse liver under light/dark cycles (Greenwell et al., 2019) and protects against obesity and metabolic syndromes in a panel of liver-specific clock mutant mice (Chaix et al., 2019). Provided the salient information on entrainment of liver physiology and metabolism by feeding rhythms, there is a gap in whether and how inverted feeding entrains diurnal oscillations of circadian clocks, physiology, and metabolism in extra-hepatic peripheral tissues.

Here, we applied inverted feeding regimens to uncouple peripheral clocks from the SCN clock and performed 24-h global profiling of transcripts and metabolites in mouse peripheral tissues to study the transition kinetics during inverted feeding, which would transit from the original phase to a 12-h shifted phase if fully entrained by feeding within a week. We first examined entrainment of tissue circadian clocks by feeding and discerned the impact of sex, duration of restricted feeding, and constant light on food entrainment. Next, phase analysis and pathway analysis of diurnal transcriptomes revealed distinct kinetics in food entrainment, which graded from fat tissue, liver, kidney, to heart, and predicted potential physiological and metabolic pathways entrained by inverted feeding. We integrated diurnal transcriptomes with metabolomes/lipidomes and revealed that fatty acid oxidation entrained almost completely to feeding, despite the slow kinetics and/or resistance of the heart clock in food entrainment. In summary, this systems approach sheds light on molecular and metabolic signatures of inverted feeding on circadian biology in peripheral tissues and provides an integrated resource to approach clock synchronization in the body.

RESULTS

Global transcript profiling of mouse tissues over 24 h reveals robust diurnal rhythms of transcriptomes under time-restricted feeding

To study food entrainment of diurnal transcriptomes in peripheral tissues, 9-week-old female mice on time-restricted feeding (tRF) regimens, namely daytime (DRF)- and nighttime (control, NRF)-restricted feeding, for one week were subjected to tissue collection, including visceral adipose tissue (VAT), liver, kidney, and heart, at a 4-h interval over 24 h (Figure 1A). Female mice were chosen because they have not been studied by multi-tissue multi-omics in tRF regimens but are known to respond to inverted feeding (Davidson et al., 2003). This one-week regimen is sufficient to entrain liver clocks in rodents (Damiola et al., 2000; Stokkan et al., 2001). Tissues were subjected to global transcript profiling (Table S1) for an average of 50 million reads with a minimal coverage of 39.6 million reads per sample. Liver, heart, and VAT were further subjected to untargeted metabolomics or targeted lipidomics for integration studies (Figure 1A). In total, we performed 224 deep RNA sequencing (Table S2), 138 untargeted metabolomics, and 48 targeted lipidomics experiments (Tables S3 and S4).

To validate the pipeline, we visualized the Dbp and Arntl (Bmal1) loci from global transcript profiling and confirmed that inverted feeding reversed the phase of Dbp rhythm in liver (Figures 1B and S1A). Inverted feeding for 1 week did not significantly alter the body weight and visceral adiposity in mice (Figure S1B). The effect on body weight is in line with a previous study (Wang et al., 2017). Wheel-running activity recording confirmed that DRF group remained active in the night, which results in a complete phase uncoupling between voluntary locomotor rhythm and feeding rhythm (Figure S1C), which is consistent with a recent study using an automated feeder system (Acosta-Rodríguez et al., 2017). Principal component analysis revealed the effects of tRF regimens on tissue multi-omics (Figure S1D). Expression levels of transcripts were subjected to MetaCycle rhythmicity analysis with Benjamini-Hochberg procedure. About 10%–30% of the transcriptome exhibit diurnal rhythms in peripheral tissues (Table S2). This is consistent with published work (Hughes et al., 2009; Zhang et al., 2014). We detected 1167–2859 diurnal genes that oscillated under both DRF and NRF regimens (Figure 1C, Table S2), which allowed phase analysis to understand transcriptome-wide phase entrainment by inverted feeding in peripheral tissues. In sum, robust diurnal rhythms of tissue transcriptomes under tRF regimens were detected by diurnal transcriptomics.

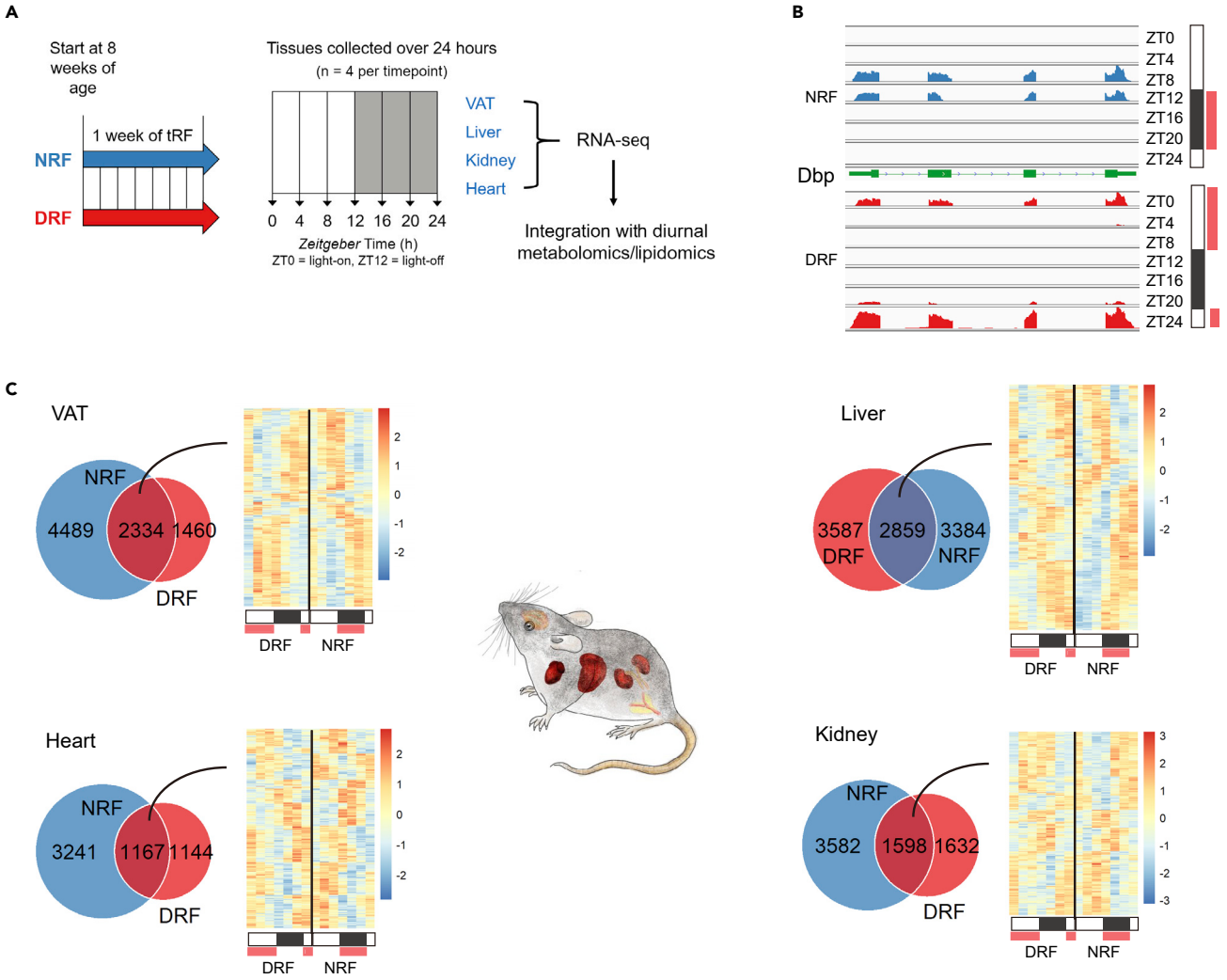

Figure 1. Global transcript profiling of mouse tissues over 24 h reveals robust diurnal rhythms of transcriptomes under time-restricted feeding

(A) The workflow of multi-omics analysis of diurnal rhythms in peripheral tissues from female mice subjected to inverted feeding for 1 week. All transcript profiles have at least 40 million reads per sample. DRF, daytime-restricted feeding; NRF, nighttime-restricted feeding; VAT, visceral adipose tissue. See transparent methods.

(B) Read counts from the clock output gene *Dbp* locus exhibit diurnal rhythms in liver and are phase inverted under DRF. ZT, zeitgeber time. See also Figures S1A and S1B.

(C) General features of the global transcript profiling of peripheral tissues in 9-week-old time-restricted-fed C57BL/6J female mice. Venn diagrams illustrate the overlap of oscillating genes between DRF and NRF in each tissue. Heatmaps show 24-h expression profiles of genes that oscillated under both DRF and NRF conditions.

Circadian clocks show tissue-specific kinetics in phase entrainment by inverted feeding

To test whether cell-autonomous circadian clocks entrained to inverted feeding with different kinetics, we examined the expression profiles of clock genes, including Nr1d1 (Rev-Erbα), Dbp, Per2, and Arntl (Bmal1). The statistical significance of changes in rhythmicity parameters was computed by CircaCompare (Parsons et al., 2020). The results showed that inverted feeding completely reversed the phase of clock genes in liver and decreased the amplitude (Figure 2A). This is consistent with previous knowledge (Reinke and Asher, 2019). In VAT, 24-h expression profiles of Nr1d1 and Dbp became arrhythmic under DRF (Figure 2B). Diurnal rhythms of Per2 and Arntl showed incomplete phase shifts by 2 h and 6 h, respectively and exhibited a large decrease of amplitude in VAT (Figure 2B). These observations suggested a dampening response of the adipose clock in phase entrainment by feeding. In kidney (Figure 2C) and heart (Figure 2D), diurnal rhythms of clock genes showed phase shifts of 0–3 h, which suggested slow kinetics and/or resistance in phase entrainment of clocks in these tissues by feeding.

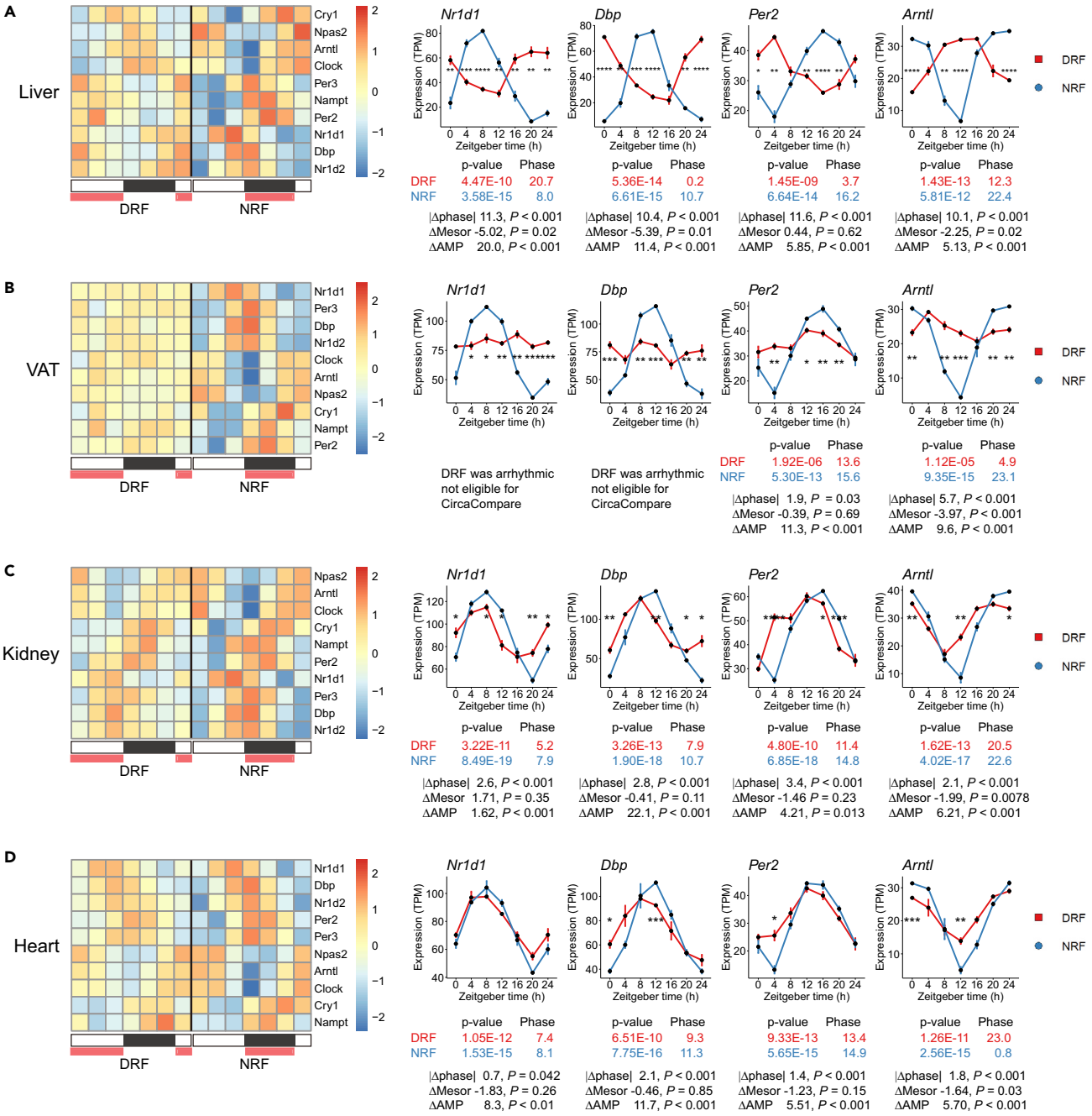

Figure 2. Circadian clocks show tissue-specific kinetics in phase entrainment by inverted feeding

(A–D) Diurnal expression of clock genes in liver (A), VAT (B), kidney (C), and heart (D). In heatmaps, expression levels are represented as Z score of the mean (n = 4). White/black blocks indicate light/dark cycle. Red frames indicate feeding period. In line-plots, samples are represented as mean ± sem (n = 4). Statistics and comparison of rhythmicity parameters were computed by CircaCompare. Mesor, rhythm-adjusted mean expression level; AMP, amplitude. Multiple t-tests with Bonferroni correction; not shown when p ≥ 0.05, *p < 0.05, **p < 0.01, ***p < 0.001, ****p < 0.0001.
See also Figure S2.

To determine whether the different kinetics in clock-entraining responses to inverted feeding are modulated by sex-related signals, we performed quantitative PCR analysis and quantified diurnal expression profiles of clock genes in male mice that had been subjected to inverted feeding for one week. As expected, diurnal rhythms of clock genes such as Nr1d1, Dbp, and Arntl entrained to

A 36-day tRF

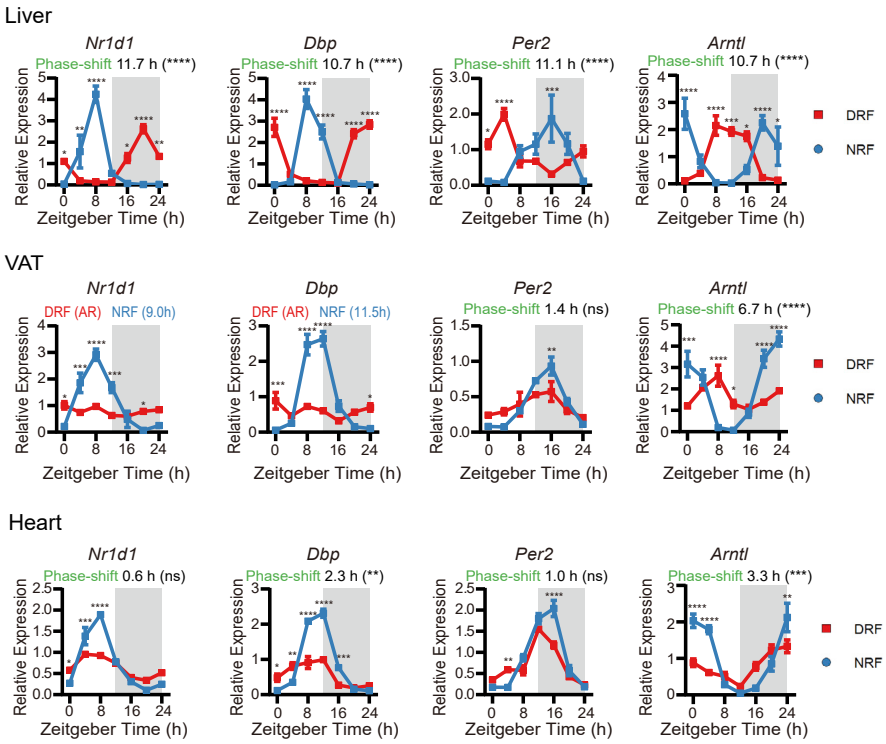

B constant lightness (LL)

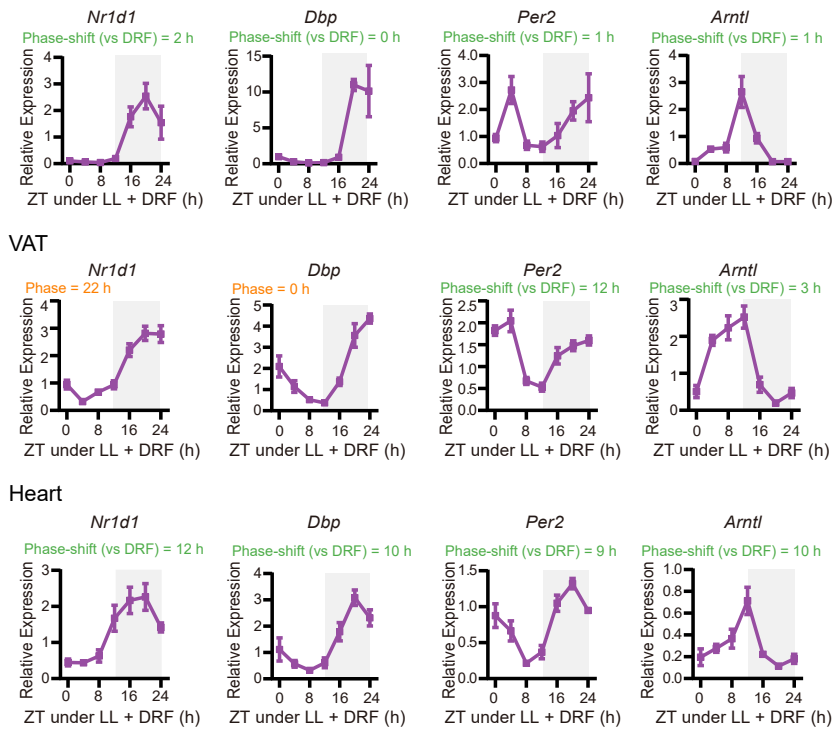

Figure 3. Effects of duration and constant light on clock entrainment by inverted feeding

(A) Effects of 36-day inverted feeding on diurnal expression of clock genes in liver, VAT, and heart. Phase shifts were computed by CircaCompare, with statistical significance from t tests indicated in the brackets. Phase parameter from MetaCycle (meta2d_phase) was shown when CircaCompare could not be applied. ns, $p \geq 0.05$, *$p < 0.05$, **$p < 0.01$, ***$p < 0.001$, ****$p < 0.0001$. See also Figures S3A–S3C.

(B) Effects of constant light (LL) on diurnal expression of clock genes in liver, VAT, and heart under DRF. Female mice were acclimated to 12-h light-dark cycles, subjected to LL for 9 days, and then subjected to DRF and LL for 7 days. Phase shift was estimated by meta2d_phase (H) with the period length under LL set to 20–28 h and that under LD set to 24 h. CircaCompare could not be applied because the period length under LL differs significantly from that under 12-h light-dark cycles. Data are represented as mean ± sem (n = 4). Multiple t tests with Bonferroni correction; not shown when $p \geq 0.05$, *$p < 0.05$, **$p < 0.01$, ***$p < 0.001$, ****$p < 0.0001$. See also Figures S3D–S3E.

inverted feeding almost completely in males (Figure S2A). Diurnal rhythm of Per2 was less robust under DRF, but the peak time as roughly 12 h apart between tRF. In VAT, diurnal rhythms of Nr1d1 and Dbp were dampened by inverted feeding (Figure S2B). Unlike in female VAT, diurnal rhythms of Per2 became dampened, whereas that of adipose Arntl was reversed by inverted feeding in male VAT (Figure S2B). In kidney, diurnal rhythms of Dbp and Arntl were phase-locked under DRF and severely impaired on amplitude (Figure S2C). Diurnal profiles of Nr1d1 and Per2 became arrhythmic under DRF. In heart, diurnal rhythms of clock genes were dampened by inverted feeding (Figure S2D). Together, the liver clock and part of the adipose clock maintained similar responses to inverted feeding between male and female mice; however, peripheral clocks in kidney and heart seemed to be less robust under DRF in males.

To determine whether clock entrainment in peripheral tissues reaches the steady state, we subjected female mice to inverted feeding for 36 days. We observed that body weight decreased slightly and transiently in the first two weeks, restored, and increased later in DRF-treated mice (Figure S3A), which is associated with a transient drop in food intake (Figure S3B). This effect is well powered by a sample size of 56 (a sample size of 26 is required to ensure a power of 0.8 when alpha = 0.05) and thus could reveal the small change of body weight and food intake. Profiling of clock genes in peripheral tissues around the clock revealed that after 36 days under tRF regimens, the phase shifts of circadian clocks were not different from that in the 7-day tRF in metabolic tissues, such as liver and VAT (Figure 3A). Although heart and kidney clocks remained phase-locked to light-dark cycles under 36-day tRF, the amplitude was clearly decreased by inverted feeding (Figures 3A and S3C). We could not rule out the possibility that heart and kidney clocks would eventually shift provided even longer tRF, but at least these peripheral clocks showed resistance to phase entrainment by feeding after 36 days of tRF. Comparison of phase kinetics between 36-day tRF and 7-day tRF clarified that clock entrainment under 7-day tRF regimens reflects tissue-specific kinetics.

Light and food are two principal time cues in the mammalian circadian clock system. To determine whether removal of time cues from the central clock would facilitate phase entrainment of peripheral clocks by feeding, we used constant light (~500 lux, LL) to desynchronize the SCN clock neurons (Chen et al., 2008; Ohta et al., 2005) and examined phase adaptation to inverted feeding in female mice under LL. Voluntary running activity analysis showed that LL significantly increased the period of behavioral rhythm by 1.7 h, and DRF did not significantly alter the period in these LL-conditioned female mice (Figure S3D, LD: 23.91 ± 0.012 h, LL: 25.61 ± 0.18 h, LL + DRF: 25.24 ± 0.55 h, mean ± sem, n = 8). Twenty-four-hour profiling of clock genes showed that LL did not alter the phase of clock genes in liver, which had already entrained to feeding (Figure 3B).

LL seemed to facilitate non-hepatic tissue clocks to entrain completely to inverted feeding. LL induced robust oscillations of adipose clock genes, including Nr1d1 and Dbp, under DRF (Figure 3B). LL facilitated complete phase inversion of Per2 and Arntl in VAT (Figure 3B). Clock genes in heart were phase inverted under DRF in LL-conditioned female mice (Figure 3B). Diurnal oscillations of Nr1d1, Dbp, and Per2 in kidney were phase inverted as well under LL + DRF; however, renal Arntl was only moderately phase shifted under LL + DRF (Figure S3E). Our results indicated that removal of the time cues from the central clock by LL promotes readily entrainment of extra-hepatic tissue clocks by feeding.

Overall, our data showed that cell-autonomous circadian clocks entrained to 7-day inverted feeding with different kinetics, which is gated by light-related cues.

Inverted feeding reverses diurnal transcriptomes in VAT and liver

To determine phase entrainment of diurnal transcriptomes in peripheral tissues, we examined phase shifts of diurnal genes that oscillated under both tRF regimens (hereafter named as dual-oscillating genes). Considering the cyclic nature of circadian rhythms, absolute value of phase shift was presented. For example, a phase delay of 14 h is equal to a phase advance of 10 h (= 24 h–14 h) and would be presented as a phase shift of 10 h. Considering the phase resolution limited by the 4-h sampling interval, we defined phase shift within 4 h (0–4 h) as the phase-locked status and phase shift between 8 and 12 h as the phase-inverted status (8–12 h).

In VAT, phase-shift histogram showed that 80.46% of dual-oscillating genes were phase inverted under DRF in VAT (Figure 4A). Adipose phase-inverted genes from DRF and NRF exhibited clusters around ZT9 and ZT20-23 (Figure S4A). Phase set enrichment analysis (PSEA) of dual-oscillating genes using Gene Ontology (GO) terms based on phase shifts revealed that highly phase-clustered pathways exhibited at least a 10-h phase-shift and enriched biological progresses such as long-chain fatty acid metabolism, RNA modification, and Golgi vesicle trafficking (Figure 4B, Table S3). Cistrome matching analysis based on published genome-wide binding sites of transcription factors (TF) and chromatin regulators in VAT found chromatin-binding signatures for histone deacetylase-dependent corepressor SIN3A, MYC, etc. near phase-inverted genes (Figure 4C). Cistrome matching analysis predicted histone acetylase EP300, and circadian regulators, such as NR3C1 (glucocorticoid receptor), HDAC3, NR1D1, and ARNTL, etc. as potential transcriptional regulators of phase-locked genes in VAT (Figure S4B).

In liver, 61% of dual-oscillating genes were phase inverted under DRF (Figure 4D). Phase-inverted genes exhibited enrichment around ZT23-0 under DRF (Figure S4C). PSEA of dual-oscillating genes based on phase shifts identified signatures of metabolism of complex carbohydrates, transport of lipids, and glucose (Figure 4E, Table S3). These metabolic pathways showed 8–11 h of phase shifts, which is consistent with existing studies (Vollmers et al., 2009; Zhang et al., 2016). Cistrome matching analysis in liver showed that circadian clock TFs, e.g. BMAL1, CRY1, CLOCK, PER2, and NR1D1, were among the TFs bound near phase-inverted genes (Figure 4F). Cistrome matching analysis showed that in the gene-set of phase-locked genes, components of RNA polymerase II, such as POLR2A and POLR2B, were among top 3 predicted chromatin-bound TFs (Figure S4D).

To explore potential dietary components driving phase entrainment of diurnal transcriptomes in liver, we performed an integrated analysis of our hepatic dataset and existing datasets of hepatic diurnal transcriptomes modulated by high-fat diet (HFD, GSE52333), ketogenic diet (KD, GSE87425), calorie restriction (CR, GSE93903), and 24-h fasting (Fasted, GSE107787). Because phase entrainment is rare in these datasets, we relaxed the threshold to include diurnal genes with a phase shift >4 h. We retrieved 2,248 phase-shifted diurnal genes in DRF, 624 in CR, 121 in Fasted, 16 in HFD, and 11 in KD (Figure 4G). About 34% (41/121) of phase-shifted diurnal genes in Fasted liver were present in DRF-treated liver, whereas only 6.4% (40/624) in CR liver were present in DRF-treated liver (Figure 4G). Considering the percentage of phase-shifted diurnal genes in dual-oscillating genes as an indicator, we found that food scarcity is positively associated with the degree of phase entrainment in hepatic diurnal transcriptomes, such as 29.66% in Fasted, 13.19% in CR, 3.96% in HFD, and 3.56% in KD (Figure 4H). The results suggested that fasting might condition phase entrainment of hepatic diurnal transcriptome under light/dark cycles.

Next, we determined phase entrainment of hepatic diurnal lncRNA-omes by feeding. We uncovered 288 diurnal lncRNA gene-derived lncRNAs in liver. About 79.1% of the 66 dual-oscillating lncRNAs were phase inverted by inverted feeding (Figures S4E and S4F), suggesting that lncRNA profiles exhibit a faster kinetics than the total transcriptome (61%) in phase entrainment. Atrolnc-1 (1110038B12Rik) is recently shown to be induced by catabolic signals, including nutrient deprivation, and contributes to muscle wasting (Sun et al., 2018). Atrolnc-1 exhibited robust entrainment to inverted feeding in liver, based on mapped reads (Figure S4G). Data mining via CirGRDB showed that diurnal oscillation of Atrolnc-1 was enabled by calorie restriction in mouse liver (peak ZT9) (Li et al., 2018; Sato et al., 2017). We confirmed the robust phase entrainment of four hepatic lncRNAs, including Atrolnc-1 by RT-qPCR analysis (Figure S4H).

In sum, diurnal transcriptomes in metabolic tissues, such as VAT and liver, entrained readily to inverted feeding. Adipose diurnal transcriptomes showed higher completeness in phase entrainment by feeding

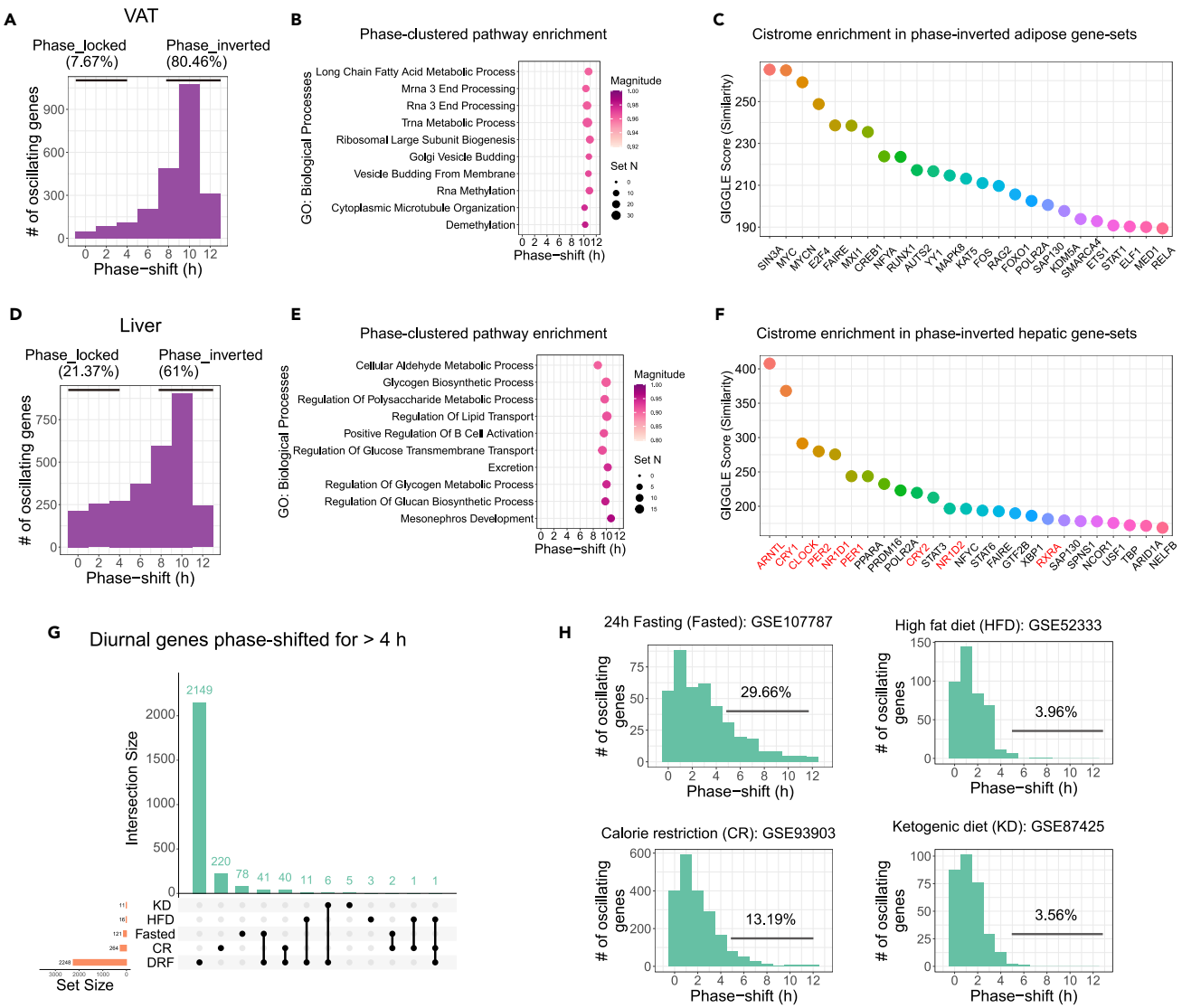

Figure 4. Inverted feeding reverses diurnal transcriptomes in VAT and liver

(A) Phase-shift histogram shows that 80.46% of the adipose dual-oscillating genes were phase inverted by inverted feeding. Phase-locked, phase shift of 0–4 h; phase-inverted, phase shift of 8–12 h. Considering the cyclic nature, phase shift is converted to absolute value to allow a window of 0–12 h, e.g. a phase advance of 14 h equals to a phase delay of 10 h (24–14 = 10), and is expressed as a phase shift of 10 h. See also Figure S4A. VAT, visceral adipose tissue.

(B) Top 10 phase-clustered pathways that are phase shifted by inverted feeding in VAT. Magnitude is a measure of the temporal cohesiveness of the phase set ($q < 0.05$).

(C) Cistrome enrichment analysis of phase-inverted genes in VAT based on curated cistromes of transcription factors and chromatin regulators from CistromeDB. Circadian clock proteins are marked in red. See also Figure S4B.

(D) Phase-shift histogram shows that 61% of the hepatic dual-oscillating genes were phase inverted by inverted feeding. See also Figure S4C.

(E) Top 10 phase-clustered pathways that are phase shifted by inverted feeding in liver.

(F) Cistrome enrichment analysis of phase-inverted genes in liver based on curated cistromes of transcription factors and chromatin regulators from CistromeDB. Circadian clock proteins are marked in red. See also Figure S4D.

(G) Interaction of diurnal transcripts in liver that shows phase modulation by various dietary treatments. KD, ketogenic diet; HFD, high-fat diet; Fasted, 24-h fasting; CR, calorie restriction. Rhythmicity is statistically thresholded at meta2d_BH.Q < 0.05. The period is set to 24 h.

(H) Phase-shift histogram shows that the degree of food scarcity is positively correlated with the degree of phase entrainment in hepatic diurnal transcriptomes. The degree of phase entrainment by diets is represented as the percentage of diurnal transcripts that were phase shifted by more than 4 h.

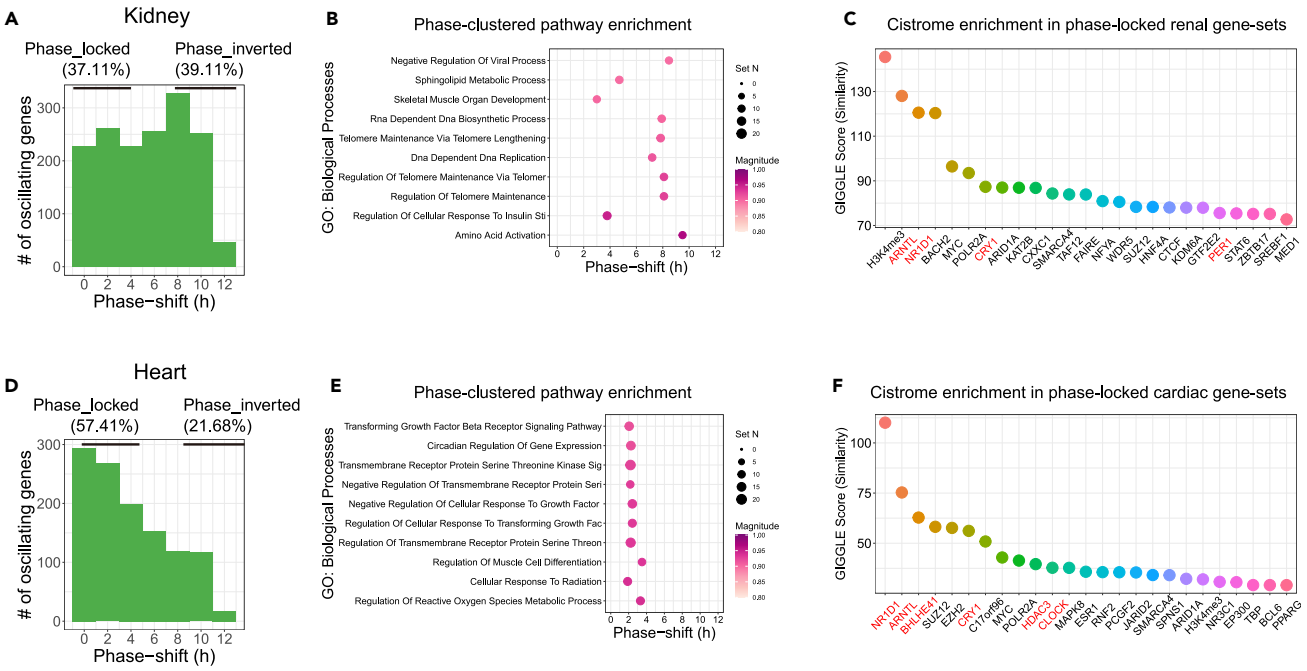

Figure 5. Diurnal transcriptomes in kidney and heart show slow kinetics/resistance in phase entrainment to feeding

(A) Phase-shift histogram shows that 39.11% of the renal dual-oscillating genes were phase inverted by inverted feeding. Phase-locked, phase shift of 0–4 h; phase-inverted, phase shift of 8–12 h. Considering the cyclic nature, phase shift is converted to absolute value to allow a window of 0–12 h, e.g. a phase advance of 14 h equals to a phase delay of 10 h (24–14 = 10), and is expressed as a phase shift of 10 h. See also Figure S5A.

(B) Top 10 phase-clustered pathways that are phase shifted by inverted feeding in kidney. Magnitude is a measure of the temporal cohesiveness of the phase set ($q < 0.05$).

(C) Cistrome enrichment analysis of phase-locked genes in kidney based on curated cistromes of transcription factors and chromatin regulators from CistromeDB. Circadian clock proteins are marked in marked. See also Figure S5B.

(D) Phase-shift histogram shows that 21.68% of the cardiac dual-oscillating genes were phase inverted by inverted feeding. See also Figure S5C.

(E) Top 10 phase-clustered pathways that are phase shifted by inverted feeding in heart.

(F) Cistrome enrichment analysis of phase-locked genes in heart based on curated cistromes of transcription factors and chromatin regulators from CistromeDB. Circadian clock proteins are marked in red. See also Figure S5D.

than hepatic diurnal transcriptomes. Signatures of circadian clock TFs were enriched in phase-locked genes in VAT and phase-inverted genes in liver.

Diurnal transcriptomes in kidney and heart show slow kinetics/resistance in phase entrainment to feeding

In kidney, 37.11% of the dual-oscillating genes remained phase locked to the light-dark cycle, whereas 39.11% were phase inverted (Figure 5A). Renal phase-inverted genes were clustered around ZT9 and ZT23 (Figure S5A). Pathway enrichment via PSEA revealed that phase-shift distribution of the ten most enriched pathways spanned from 4 h (cellular response to insulin stimulation), 6 h (telomere biology), to 9–10 h (amino acid activation) (Figure 5B, Table S3). Cistrome matching analysis showed that circadian TFs and histone H3 lysine 4 trimethylation (H3K4me3) were among top TFs and histone marks enriched in the vicinity of phase-locked genes (Figure 5C), whereas PPARA, FOXO1, etc. were among the top TFs bound to phase-inverted genes (Figure S5B).

In heart, the majority (57.41%) of dual-oscillating genes were phase locked to light-dark cycles, and only 21.68% of genes were phase inverted by inverted feeding (Figure 5D). Phase-inverted genes were clustered around ZT0 and ZT9, respectively (Figure S5C). PSEA revealed that almost all top 10 enriched pathways, including circadian clock, redox metabolism, and TGFβ signaling, remained phase locked to light/dark cycles (Figure 5E, Table S3). To explore regulatory mechanisms, we performed cistrome-matching analysis and found that circadian clock transcription factors, (e.g. NR1D1, ARNTL, BHLHE41, and CRY1) and components of polycomb repressive complex 2 (e.g. SUZ12 and EZH2) were top predicted TFs governing the

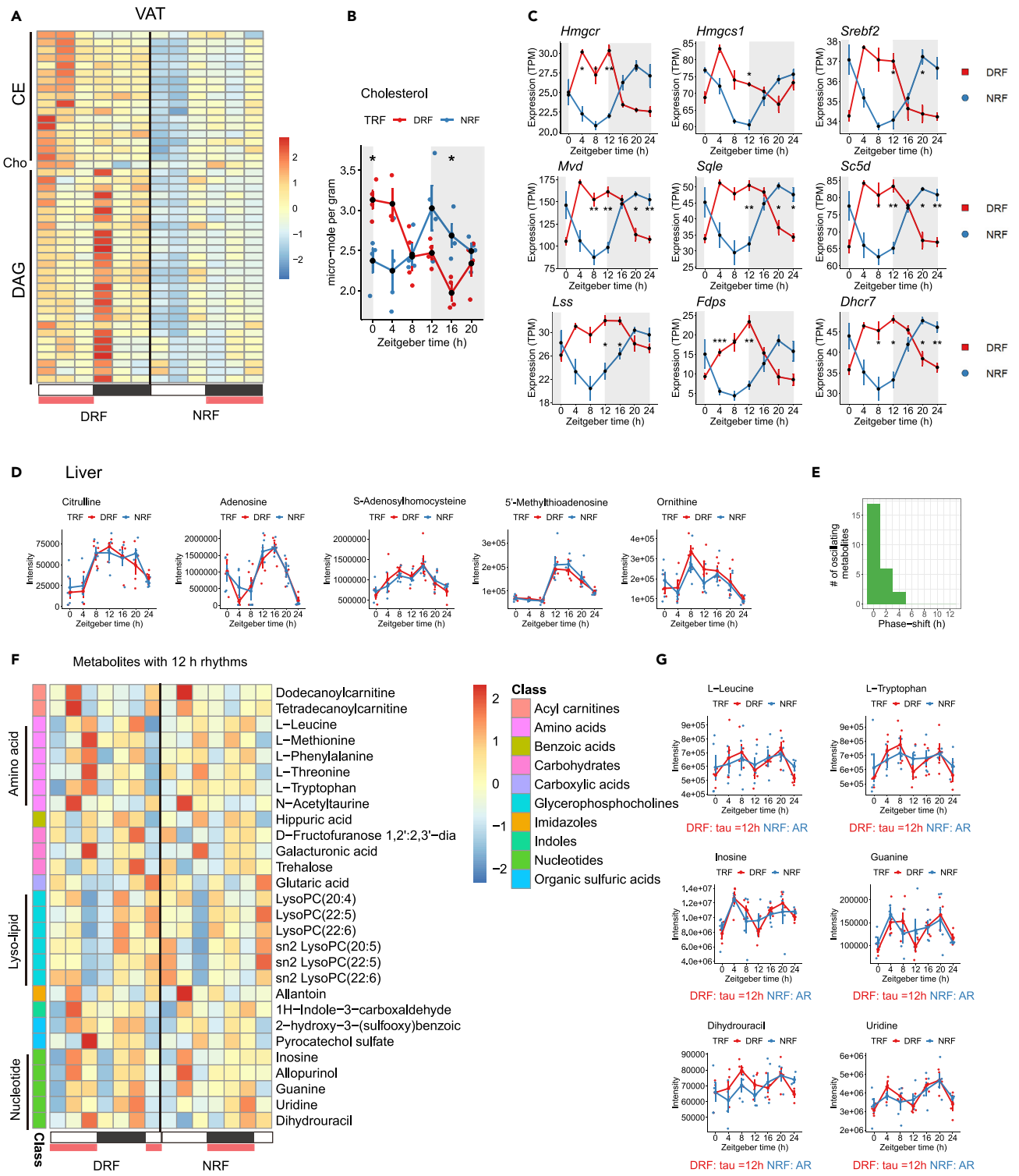

Figure 6. Phase entrainment of diurnal lipidomes and metabolomes in VAT and liver by inverted feeding

(A) Heatmap showing 24 h profiles of neutral lipids by targeted lipidomics in VAT. Cho, cholesterol. See also Figures S6A and S6B.

(B) Cholesterol rhythm is reversed by inverted feeding in VAT. Data were represented as mean ± sem (n = 4 except n = 3 in DRF ZT4 group).

(C) Diurnal expression of genes in cholesterol biosynthesis process is reversed by inverted feeding in VAT. See also Figure S6C.

(D) Twenty-four-hour profiles of representative diurnal metabolites in liver under tRF regimens. See also Figure S6D.

Figure 6. *Continued*

(E) Phase-shift diagram of dual-oscillating metabolites in liver.

(F) Heatmap showing 24 h of hepatic metabolites with 12-h rhythms. These metabolites oscillated under at least one tRF regimen.

(G) Twenty-four-hour profiles of representative hepatic metabolites with 12-h rhythms under tRF regimens. Tau, the period length. Data were represented as mean ± sem (n = 4–5 for metabolites, n = 4 for genes). Multiple t tests with Bonferroni correction; $p \geq 0.05$ is not shown, *$p < 0.05$, **$p < 0.01$, ***$p < 0.001$.

phase-locked gene sets (Figure 5F), whereas FOXK1, FOXO1 and CREB1 were among top TFs bound to phase-inverted genes (Figure S5D). We tested the robustness of the chronotype in heart in an independent cohort (n = 1, sampled every 4 h for 24 h) and reproduced the findings on slow kinetics and/or resistance in phase entrainment by feeding (Figure S5E).

In sum, diurnal transcriptomes in kidney and heart showed slow kinetics and/or resistance in phase entrainment by inverted feeding. Cardiac diurnal transcriptomes exhibited lower completeness in phase entrainment than renal diurnal transcriptomes. Phase-locked genes in these tissues enriched signatures of circadian clock TFs.

Phase entrainment of diurnal lipidomes and metabolomes in VAT and liver by inverted feeding

To match our findings in diurnal transcriptomes in metabolic tissues, we assessed phase entrainment of diurnal lipidomes in VAT and diurnal metabolomes in liver using targeted lipidomics and untargeted metabolomics, respectively.

In VAT, targeted lipidomics profiling of 199 neutral lipids showed that only five species oscillated in a diurnal manner under tRF regimens, which are composed of free cholesterol (Cho) and some cholesterol esters (CE) (Figure 6A, Table S4). Cholesterol rhythm was robust under DRF (Figure 6B, $p < 0.0001$, phase 2 h). Apparently, cholesterol rhythm under NRF reached the peak around 12 h. PSEA and diurnal expression profiles of cholesterol biosynthetic genes revealed that cholesterol biosynthetic process was significantly enriched (q-value 0, magnitude 0.85) and phase shifted by 10 h (Figures 6C, Table S3). We noticed and confirmed by MetaCycle rhythmicity analysis that diacylglycerol (DAG) species exhibited a 12-h oscillation under DRF (Figure S6A, Table S4). Triacylglycerol (TAG) species were not oscillating in adipose tissue but showed high levels at ZT8 under DRF (Figure S6B). By integrating with the gene panel on triglyceride metabolism, the alterations on daily profiles of DAG/TAG were associated with phase inversion of Dgat1 and Lipe (HSL) rhythms (Figure S6C). Thus, our integrated analysis of adipose lipidomes and transcriptomes showed that cholesterol rhythm entrained readily to inverted feeding, and DAG levels were induced to oscillate in a 12-h manner under DRF in VAT.

In liver, untargeted metabolomics analysis uncovered diurnal rhythms in 68 out of 243 metabolites in liver (Figure S6D). These diurnal metabolites include robust circadian metabolites in liver, e.g. citrulline, adenosine, S-adenosylhomocysteine (SAH), 5′-methylthioadenosine, and ornithine (Figure 6D). All of the 25 dual-oscillating metabolites remained phase locked to light-dark cycle (Figure 6E, Table S4). However, we detected 28 metabolites that oscillated in a 12-h rhythm, which include amino acids, lyso-lipids, and nucleotide/nucleosides (Figure 6F). Apparently, metabolites involved in amino acid metabolism and nucleotide metabolism oscillated only under DRF (Figure 6F, Table S4), such as L-leucine, L-tryptophan, inosine, guanine, dihydrouracil, and uridine (Figure 6G). Metabolites related to lyso-lipids oscillated only under NRF (Table S4). This metabolic signature suggested that diurnal rhythms of some metabolic pathways in liver were not entrained by feed-fast cycle. Instead, inverted feeding licensed the 12-h oscillations of metabolites related to amino acids and nucleotides in liver.

Inverted feeding entrains diurnal rhythms of fatty acid oxidation in heart

To determine how inverted feeding entrains diurnal physiology and metabolism in heart, we integrated diurnal transcriptomes and metabolomes in heart tissue. Untargeted metabolomics analysis of diurnal metabolites in heart uncovered 113 diurnal metabolites (Figure S7, Table S4). Clustering analysis based on diurnal profiles of these metabolites under both tRF regimens produced six clusters of metabolites. Particularly, cluster 3 metabolites are mainly composed of acylcarnitines and some metabolites in nucleotide metabolism and energy metabolism (Figure S7). We further found that inverted feeding reversed diurnal rhythms of the 41 dual-oscillating diurnal metabolites in heart tissue, including three major classes, such as acylcarnitine, amino acid, and nucleotide (Figure 7A). Phase-inverted metabolites accounted for

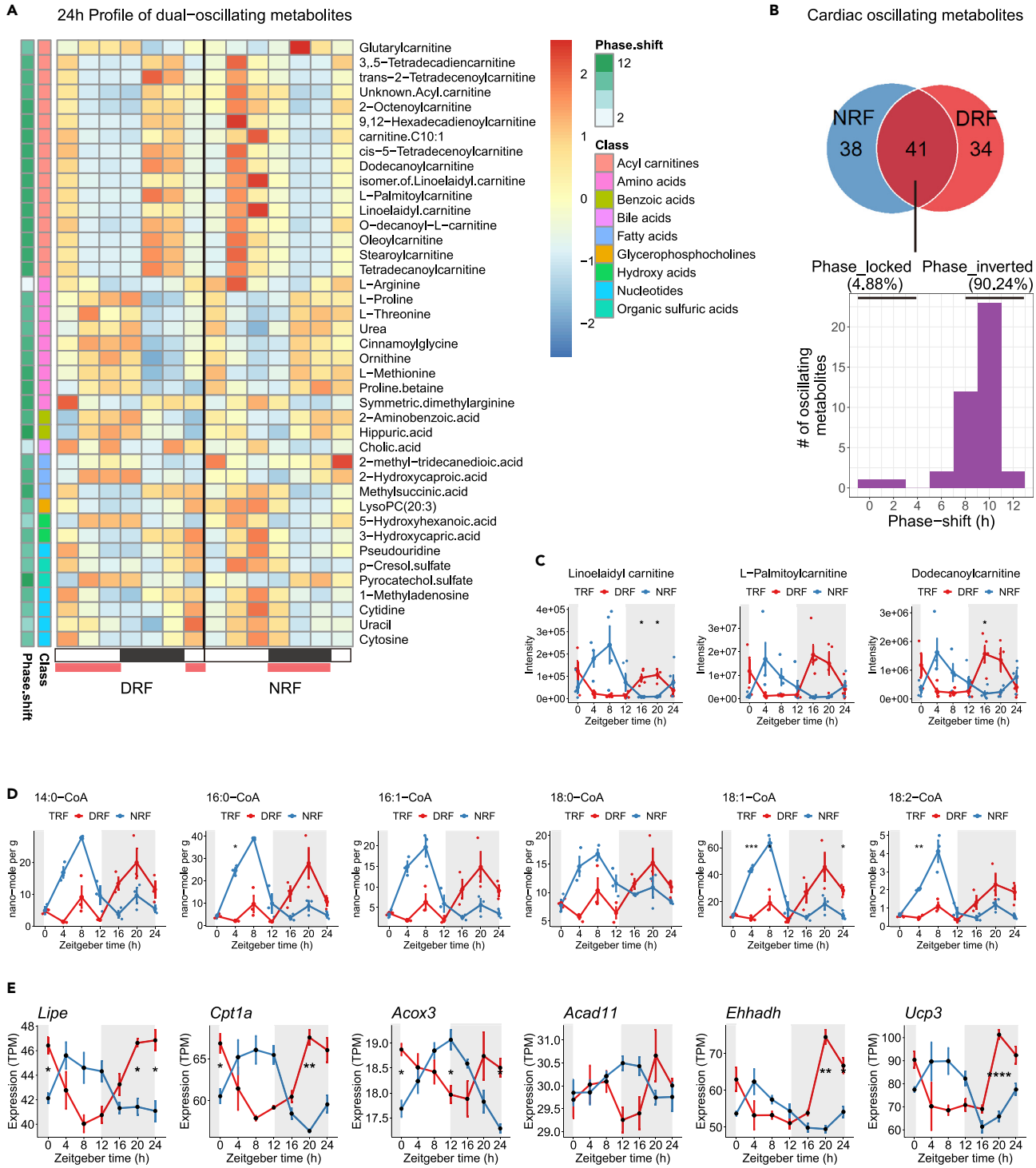

Figure 7. Inverted feeding entrains diurnal rhythms of fatty acid oxidation in heart

(A) Heatmap showing 24-h profiles of all dual-oscillating metabolites in heart. Intensity levels are represented as the Z score scaled means. See Figure S7A.

(B) Venn diagram and phase-shift diagram showing the interaction between diurnal metabolites in heart under tRF regimens, 90.24% of which were phase inverted.

(C) Representative 24-h profiles of acylcarnitines in heart.

(D) Twenty-four-hour targeted lipidomics profiles of long-chain acyl-CoAs in heart.

(E) Twenty-four-hour expression profiles of diurnal genes involved in fatty acid oxidation. Red, DRF; blue, NRF. Data were represented as mean ± sem (n = 4 for genes, n = 4–5 for metabolites, n = 3 for acyl-CoAs). Multiple t tests with Bonferroni correction; $p \geq 0.05$ is not shown, *$p < 0.05$, **$p < 0.01$, ***$p < 0.001$.

90.24% of the dual-oscillating metabolites (Figure 7B). Thus, despite the slow kinetics and/or resistance in phase entrainment of cardiac transcriptomes by feeding, inverted feeding entrained diurnal metabolomes in heart readily within one week.

Fatty acid oxidation is key to maintain energy metabolism and tissue homeostasis in heart. As shown in Figure 7C, the peak time of cardiac acylcarnitine species fell in the inactive/food-restricted period, reflecting the priority of fat burning in the postprandial phase in heart tissue. Targeted lipidomics profiling of acyl-CoA species showed that inverted feeding reversed the phase of cardiac acyl-CoA species in synchrony with its actions on acylcarnitines (Figure 7D, Table S4). These coordinated entrainment of substrates and intermediates of fatty acid oxidation by inverted feeding is associated with transcriptional changes. Diurnal rhythms of major genes involved in lipolysis and fatty acid oxidation, such as Lipe, Cpt1a, Acox3, Acad11, Ehhadh, and Ucp3, were phase inverted by inverted feeding in heart (Figure 7E).

In summary, diurnal metabolome of the heart is readily responsive to phase entrainment by feeding, particularly regarding metabolites involved in fatty acid oxidation. This metabolic reprogramming by feeding time is coordinated with fast kinetics in entraining transcriptional rhythms of fatty acid oxidative genes to feed-fast cycles in heart.

DISCUSSION

We took a multi-omics approach to study entrainment of diurnal rhythms and circadian clocks by inverted feeding in mouse peripheral tissues. Diurnal transcriptomics revealed tissue-specific kinetics in phase entrainment by feeding. Metabolic tissues, such as fat tissue (80.46% of dual-oscillating genes) and liver (61%) entrained readily to inverted feeding, whereas kidney (39.11%) and heart (21.68%) exhibited less completeness in food entrainment within one week of inverted feeding. We further showed that light-related cues condition phase entrainment of clocks by feeding in extra-hepatic peripheral tissues. To explore the impact on physiology and metabolism, we performed integrated analysis of metabolites, lipids, and transcripts and found that cholesterol rhythm entrained readily to inverted feeding in fat tissue and that diurnal rhythms of fatty acid oxidation entrained almost completely to inverted feeding in heart, both of which occurred with coordinated entrainment of metabolic gene transcripts.

In the past, much has been focused on entrainment of the liver clock by feeding. Nutrient-sensing pathways, such as glucose-sensing AMPK/OGT, NAD^+-sensing sirtuins/PARP1, and PGC-1α, couple circadian clocks to nutrient availability (Kim and Lazar, 2020; Reinke and Asher, 2019). Feeding rhythms accounted for 84% of phase-shifted transcripts in mouse liver under constant darkness (Vollmers et al., 2009). Early studies suggested that tissue clocks might entrain to feeding rhythms with different speeds (Damiola et al., 2000; Stokkan et al., 2001). Recently, Wang et al. showed that tRF shifted the phase of the skin clock by 3–4 h (Wang et al., 2017). In our study, we found distinct kinetics in entrainment of diurnal transcriptomes and tissue clocks by feeding. Metabolic tissues exhibited faster kinetics, whereas heart and kidney had slower kinetics. This effect tracks with phase kinetics of tissue clocks. These findings suggested that the connection between clock and metabolism is highly tissue specific. It is tempting to speculate that the desynchrony of diurnal transcriptomes among peripheral tissues under irregular eating time may contribute to the pathogenesis of metabolic diseases, in addition to the well-recognized desynchrony between the SCN clock and peripheral clocks (Longo and Panda, 2016; Rubino et al., 2020).

Feed-fast cycles provide a dominant synchronizing signal to reset the liver clock. Recent studies suggested that peripheral clocks in liver and skin were modulated by light-dependent signaling and clocks in other tissues (Koronowski et al., 2019; Ray et al., 2020; Welz et al., 2019). Our results are consistent with these findings and show that light-related cues gate clock entrainment in peripheral tissues. Particularly, removal of time cues from the SCN clock by LL either consolidates or facilitates phase entrainment by feeding in extra-hepatic tissues. The identity of light-related signaling under tRF remains to be characterized. It has been shown that the hypothalamus-pituitary-adrenal axis, sympathetic tones, and body temperature-sensitive signaling entrain the liver clock from the light-responsive SCN clock (Liu et al., 2019; Schibler et al., 2016). Thus, a tissue-specific balancing act between light- and food-induced signaling pathways may determine the kinetics in entrainment of peripheral clocks and diurnal rhythms by feeding.

Female mice have not been widely used in tRF studies. Our study used female mice for multi-omics profiling and compared entrainment of peripheral clocks between females and males. We observed sex-related

difference in the robustness of peripheral clocks under DRF, particularly in heart and kidney. It has been recognized recently that behavioral rhythms are more consolidated in females than in males (Anderson and FitzGerald, 2020). Weger et al. showed that not all but about 71% diurnal transcripts and 55% diurnal metabolites in liver are conserved between male and female mice, which is conditioned by microbiome (Weger et al., 2019). Thus, this resource could serve as a primer to explore mechanisms underneath sexual dimorphism in food entrainment, which may have implications for susceptibility of males to metabolic diseases.

The landscape of circadian physiology and metabolism entrained by feeding is key to understand the mechanisms and health benefits of tRF. In heart, we found coordinated phase entrainment of fatty acid metabolic genes and acylcarnitine metabolites. It is well established that the myocardial circadian clock regulates diurnal rhythms of mitochondrial oxidative metabolism and fatty acid utilization in heart, which is essential for longevity and health span (Zhang et al., 2020a). Clock-regulated transcription factor KLF15 conditions diurnal rhythms of susceptibility to heart injury, in part through fatty acid metabolism and electrophysiology (Jeyaraj et al., 2012; Li et al., 2020; Zhang et al., 2015a). These findings corroborated the notion that the circadian coherence of energy metabolism in heart is shaped by feed-fast cycles and circadian clocks. Because circadian reprogramming of fatty acid metabolism occurs prior to transcriptional changes of the circadian clock, it is likely that post-transcriptional regulation of fatty acid metabolism, possibly at the levels of proteins and activity, may account for diurnal rhythms of cardiac energy metabolism under tRF. In that sense, circadian profiling of proteomes and/or proteomes of a specific post-translational modification in heart would provide mechanistic insights in the future.

In adipose, we found robust phase entrainment of free cholesterol in synchrony with genes in cholesterol biosynthetic process. It is perplexing because VAT is not a major organ for cholesterol biosynthesis (Luo et al., 2020). The apparent clock-independent phase entrainment in VAT suggested that fat tissue might utilize an unconventional mechanism during food entrainment, which may recruit non-clock TFs such as nuclear receptors and sterol response element-binding proteins as suggested in recent studies (Eckel-Mahan et al., 2013; Guan et al., 2018; Yang et al., 2006; Zhang et al., 2015b). In liver, we did not find any diurnal metabolite that had entrained to inverted feeding; however, we found robust 12-h rhythms in many amino acids and nucleotides, including leucine. As an activator of mTOR signaling, this 12-h tone of leucine may orchestrate diurnal rhythms of metabolism and physiology via protein phosphorylation as suggested recently (Robles et al., 2017). In addition, signaling metabolites with 24 h or 12 h rhythms modulated by DRF may act not only in local tissues but also in dialogue between tissues (Dyar et al., 2018; Koronowski and Sassone-Corsi, 2021). Thus, this multi-tissue resource would facilitate the community to explore the functions of tissue-specific signature transcripts and metabolites connecting feed-fast cycles and circadian biology.

Limitations of study

Our study has several limitations. First, we have only examined four peripheral tissues. Inclusion of additional organs in other physiological systems, such as respiratory system, gastrointestinal system, endocrine system, nervous system, and musculoskeletal system, would be necessary to explore system-wide kinetics and regulatory mechanisms in entrainment of circadian biology by feeding. Second, transcriptomics and metabolomics are merely snap-shots of transcription and metabolism. To uncover the dynamics and kinetics, applications such as Global Run-On sequencing (GRO-seq) and metabolic flux analysis would be required.

Resource availability

Lead contact

Further information and requests for resources and reagents should be directed to and will be fulfilled by the lead contact, Min-Dian Li (mindianli@tmmu.edu.cn).

Materials availability

This study did not generate new reagents.

Data and code availability

Original/source data and code for metabolomics and Figures in the paper are available [i.e., Mendeley Data https://doi.org/10.17632/mb25x9t4m7.1]. The accession numbers for the transcriptomics data reported in this paper are NCBI GEO: GSE150380, GSE150381, GSE151221, GSE151228, and

CNGBdb: CNP0001605, CNP0001638, CNP0001639, CNP0001640. CircaMet database: https://www.CircaMetDB.org.cn.

METHODS

All methods can be found in the accompanying transparent methods supplemental file.

SUPPLEMENTAL INFORMATION

Supplemental information can be found online at https://doi.org/10.1016/j.isci.2021.102335.

ACKNOWLEDGMENTS

This work was supported by National Natural Science Foundation of China Grants 92057109, 81900776 to ML, 81873663 to ZZ, by a start-up fund (#4174E9) to ML, and People's Liberation Army Youth Training Project for Medical Science 20QNPY020 to FD. We thank X. Yang, C. Lee, Y. Xu, Y. Tian, Z. She, H. Chen, and S. Chen for critiques and suggestions, Qing Chen for access to ClockLab system, and Lan Wang and Yanli Wu for administrative assistance.

AUTHOR CONTRIBUTIONS

Conceptualization, H.X., F.D., Z.Z., and M.L.; Methodology, H.X., H.T., G.S., and M.L.; Investigation, H.X., X.M., Z.M., H.R., H.T., Y.T., X.C., D.D., S.G., F.D., Z.Z., and M.L.; Formal Analysis, H.X. and M.L.; Data Curation, H.X. and M.L.; Visualization, H.X. and M.L.; Writing—Original Draft, H.X. and M.L.; Writing—Review & Editing, H.X., X.M., H.T., G.S., F.D., Z.Z., and M.L.; Resources, S.G., F.D., Z.Z., and M.L.; Supervision, M.L. and Z.Z..; Project Administration, F.D. and M.L.; Funding Acquisition, F.D., Z.Z., and M.L.

DECLARATION OF INTERESTS

The authors declare no competing interests.

Received: February 8, 2021
Revised: February 26, 2021
Accepted: March 16, 2021
Published: April 23, 2021

REFERENCES

Acosta-Rodríguez, V.A., de Groot, M.H.M., Rijo-Ferreira, F., Green, C.B., and Takahashi, J.S. (2017). Mice under caloric restriction self-impose a temporal restriction of food intake as revealed by an automated feeder system. Cell Metab. *26*, 267–277.e2.

Anderson, S.T., and FitzGerald, G.A. (2020). Sexual dimorphism in body clocks. Science *369*, 1164–1165.

Asher, G., Reinke, H., Altmeyer, M., Gutierrez-Arcelus, M., Hottiger, M.O., and Schibler, U. (2010). Poly(ADP-Ribose) polymerase 1 participates in the phase entrainment of circadian clocks to feeding. Cell *142*, 943–953.

Bass, J., and Lazar, M.A. (2016). Circadian time signatures of fitness and disease. Science *354*, 994–999.

Chaix, A., Lin, T., Le, H.D., Chang, M.W., and Panda, S. (2019). Time-restricted feeding prevents obesity and metabolic syndrome in mice lacking a circadian clock. Cell Metab. *29*, 303–319.e4.

Chen, R., Seo, D.O., Bell, E., Von Gall, C., and Lee, D.C. (2008). Strong resetting of the mammalian clock by constant light followed by constant darkness. J. Neurosci. *28*, 11839–11847.

Crosby, P., Hamnett, R., Putker, M., Hoyle, N.P., Reed, M., Karam, C.J., Maywood, E.S., Stangherlin, A., Chesham, J.E., Hayter, E.A., et al. (2019). Insulin/IGF-1 drives PERIOD synthesis to entrain circadian rhythms with feeding time. Cell *177*, 896–909.e20.

Damiola, F., Le Minli, N., Preitner, N., Kornmann, B., Fleury-Olela, F., and Schibler, U. (2000). Restricted feeding uncouples circadian oscillators in peripheral tissues from the central pacemaker in the suprachiasmatic nucleus. Genes Dev. *14*, 2950–2961.

Davidson, A.J., Poole, A.S., Yamazaki, S., and Menaker, M. (2003). Is the food-entrainable circadian oscillator in the digestive system? Genes Brain Behav. *2*, 32–39.

Dibner, C., Schibler, U., and Albrecht, U. (2010). The mammalian circadian timing system: organization and coordination of central and peripheral clocks. Annu. Rev. Physiol. *72*, 517–549.

Dyar, K.A., Lutter, D., Artati, A., Ceglia, N.J., Liu, Y., Armenta, D., Jastroch, M., Schneider, S., de Mateo, S., Cervantes, M., et al. (2018). Atlas of circadian metabolism reveals system-wide coordination and communication between clocks. Cell *174*, 1571–1585.

Eckel-Mahan, K.L., Patel, V.R., De Mateo, S., Orozco-Solis, R., Ceglia, N.J., Sahar, S., Dilag-Penilla, S.A., Dyar, K.A., Baldi, P., and Sassone-Corsi, P. (2013). Reprogramming of the circadian clock by nutritional challenge. Cell *155*, 1464–1478.

Greco, C.M., and Sassone–Corsi, P. (2019). Circadian blueprint of metabolic pathways in the brain. Nat. Rev. Neurosci. *20*, 71–82.

Greenwell, B.J., Trott, A.J., Beytebiere, J.R., Pao, S., Bosley, A., Beach, E., Finegan, P., Hernandez, C., and Menet, J.S. (2019). Rhythmic food intake drives rhythmic gene expression more potently than the hepatic circadian clock in mice. Cell Rep. *27*, 649–657.e5.

Guan, D., Xiong, Y., Borck, P.C., Jang, C., Doulias, P.-T.T., Papazyan, R., Fang, B., Jiang, C., Zhang, Y., Briggs, E.R., et al. (2018). Diet-induced circadian enhancer remodeling synchronizes opposing hepatic lipid metabolic processes. Cell *174*, 831–842.e12.

Hirano, A., Fu, Y.H., and Ptáek, L.J. (2016). The intricate dance of post-translational modifications in the rhythm of life. Nat. Struct. Mol. Biol. *23*, 1053–1060.

Hughes, M.E., DiTacchio, L., Hayes, K.R., Vollmers, C., Pulivarthy, S., Baggs, J.E., Panda, S., and Hogenesch, J.B. (2009). Harmonics of circadian gene transcription in mammals. PLoS Genet. *5*, e1000442.

Jeyaraj, D., Haldar, S.M., Wan, X., McCauley, M.D., Ripperger, J.A., Hu, K., Lu, Y., Eapen, B.L., Sharma, N., Ficker, E., et al. (2012). Circadian rhythms govern cardiac repolarization and arrhythmogenesis. Nature *483*, 96–101.

Kaasik, K., Kivimäe, S., Allen, J.J., Chalkley, R.J., Huang, Y., Baer, K., Kissel, H., Burlingame, A.L., Shokat, K.M., Ptáček, L.J., and Fu, Y.-H. (2013). Glucose sensor O-GlcNAcylation coordinates with phosphorylation to regulate circadian clock. Cell Metab. *17*, 291–302.

Kim, Y.H., and Lazar, M.A. (2020). Transcriptional control of circadian rhythms and metabolism: a matter of time and space. Endocr. Rev. *41*, 707–732.

Kinouchi, K., and Sassone-Corsi, P. (2020). Metabolic rivalry: circadian homeostasis and tumorigenesis. Nat. Rev. Cancer *20*, 645–661.

Koronowski, K.B., Kinouchi, K., Welz, P.S., Smith, J.G., Zinna, V.M., Shi, J., Samad, M., Chen, S., Magnan, C.N., Kinchen, J.M., et al. (2019). Defining the independence of the liver circadian clock. Cell *177*, 1448–1462.e14.

Koronowski, K.B., and Sassone-Corsi, P. (2021). Communicating clocks shape circadian homeostasis. Science *371*, eabd0951.

Krishnaiah, S.Y., Wu, G., Altman, B.J., Growe, J., Rhoades, S.D., Coldren, F., Venkataraman, A., Olarerin-George, A.O., Francey, L.J., Mukherjee, S., et al. (2017). Clock regulation of metabolites reveals coupling between transcription and metabolism. Cell Metab. *25*, 961–974.e4.

Li, L., Li, H., Tien, C.-L., Jain, M.K., and Zhang, L. (2020). Kruppel-like factor 15 regulates the circadian susceptibility to ischemia reperfusion injury in the heart. Circulation *141*, 1427–1429.

Li, M.-D., Ruan, H.-B., Hughes, M.E., Lee, J.-S., Singh, J.P., Jones, S.P., Nitabach, M.N., and Yang, X. (2013). O-GlcNAc signaling entrains the circadian clock by inhibiting BMAL1/CLOCK ubiquitination. Cell Metab. *17*, 303–310.

Li, X., Shi, L., Zhang, K., Wei, W., Liu, Q., Mao, F., Li, J., Cai, W., Chen, H., Teng, H., et al. (2018). CirGRDB: a database for the genome-wide deciphering circadian genes and regulators. Nucleic Acids Res. *46*, D64–D70.

Liu, Z., Qian, M., Tang, X., Hu, W., Sun, S., Li, G., Zhang, S., Meng, F., Cao, X., Sun, J., et al. (2019). SIRT7 couples light-driven body temperature cues to hepatic circadian phase coherence and gluconeogenesis. Nat. Metab. *1*, 1141–1156.

Longo, V.D., and Panda, S. (2016). Fasting, circadian rhythms, and time-restricted feeding in healthy lifespan. Cell Metab. *23*, 1048–1059.

Luo, J., Yang, H., and Song, B.-L. (2020). Mechanisms and regulation of cholesterol homeostasis. Nat. Rev. Mol. Cell Biol. *21*, 225–245.

Ohta, H., Yamazaki, S., and McMahon, D.G. (2005). Constant light desynchronizes mammalian clock neurons. Nat. Neurosci. *8*, 267–269.

Panda, S. (2016). Circadian physiology of metabolism. Science *354*, 1008–1015.

Parsons, Rex, Parsons, Richard, Garner, N., Oster, H., and Rawashdeh, O. (2020). CircaCompare: a method to estimate and statistically support differences in mesor, amplitude and phase, between circadian rhythms. Bioinformatics *36*, 1208–1212.

Patke, A., Young, M.W., and Axelrod, S. (2020). Molecular mechanisms and physiological importance of circadian rhythms. Nat. Rev. Mol. Cell Biol. *21*, 67–84.

Ray, S., Valekunja, U.K., Stangherlin, A., Howell, S.A., Snijders, A.P., Damodaran, G., and Reddy, A.B. (2020). Circadian rhythms in the absence of the clock gene Bmal1. Science *367*, 800–806.

Reinke, H., and Asher, G. (2019). Crosstalk between metabolism and circadian clocks. Nat. Rev. Mol. Cell Biol. *20*, 227–241.

Robles, M.S., Humphrey, S.J., and Mann, M. (2017). Phosphorylation is a central mechanism for circadian control of metabolism and physiology. Cell Metab. *25*, 118–127.

Rubino, F., Puhl, R.M., Cummings, D.E., Eckel, R.H., Ryan, D.H., Mechanick, J.I., Nadglowski, J., Ramos Salas, X., Schauer, P.R., Twenefour, D., et al. (2020). Joint international consensus statement for ending stigma of obesity. Nat. Med. *26*, 485–497.

Sato, S., Solanas, G., Peixoto, F.O., Bee, L., Symeonidi, A., Schmidt, M.S., Brenner, C., Masri, S., Benitah, S.A., and Sassone-Corsi, P. (2017). Circadian reprogramming in the liver identifies metabolic pathways of aging. Cell *170*, 664–677.e11.

Schibler, U., Gotic, I., Saini, C., Gos, P., Curie, T., Emmenegger, Y., Sinturel, F., Gosselin, P., Gerber, A., Fleury-Olela, F., et al. (2016). Clock-Talk: interactions between central and peripheral circadian oscillators in mammals. Cold Spring Harb. Symp. Quant. Biol. *80*, 223–232.

Stokkan, K.-A., Yamazaki, S., Tei, H., Sakaki, Y., and Menaker, M. (2001). Entrainment of the circadian clock in the liver by feeding. Science *291*, 490–493.

Sun, L., Si, M., Liu, X., Choi, J.M., Wang, Y., Thomas, S.S., Peng, H., and Hu, Z. (2018). Long-noncoding RNA Atrolnc-1 promotes muscle wasting in mice with chronic kidney disease. J. Cachexia Sarcopenia Muscle *9*, 962–974.

Takahashi, J.S. (2017). Transcriptional architecture of the mammalian circadian clock. Nat. Rev. Genet. *18*, 164–179.

Vollmers, C., Gill, S., DiTacchio, L., Pulivarthy, S.R., Le, H.D., and Panda, S. (2009). Time of feeding and the intrinsic circadian clock drive rhythms in hepatic gene expression. Proc. Natl. Acad. Sci. U S A *106*, 21453–21458.

Wang, H., van Spyk, E., Liu, Q., Geyfman, M., Salmans, M.L., Kumar, V., Ihler, A., Li, N., Takahashi, J.S., and Andersen, B. (2017). Time-restricted feeding shifts the skin circadian clock and alters UVB-induced DNA damage. Cell Rep. *20*, 1061–1072.

Weger, B.D., Gobet, C., Yeung, J., Martin, E., Jimenez, S., Betrisey, B., Foata, F., Berger, B., Balvay, A., Foussier, A., et al. (2019). The mouse microbiome is required for sex-specific diurnal rhythms of gene expression and metabolism. Cell Metab. *29*, 362–382.e8.

Welz, P.S., Zinna, V.M., Symeonidi, A., Koronowski, K.B., Kinouchi, K., Smith, J.G., Guillén, I.M., Castellanos, A., Crainiciuc, G., Prats, N., et al. (2019). BMAL1-Driven tissue clocks respond independently to light to maintain homeostasis. Cell *177*, 1436–1447.

Yang, X., Downes, M., Yu, R.T., Bookout, A.L., He, W., Straume, M., Mangelsdorf, D.J., and Evans, R.M. (2006). Nuclear receptor expression links the circadian clock to metabolism. Cell *126*, 801–810.

Yang, X., and Qian, K. (2017). Protein O-GlcNAcylation: emerging mechanisms and functions. Nat. Rev. Mol. Cell Biol. *18*, 452–465.

Zhang, J., Chatham, J.C., and Young, M.E. (2020a). Circadian regulation of cardiac physiology: rhythms that keep the heart beating. Annu. Rev. Physiol. *82*, 79–101.

Zhang, L., Prosdocimo, D.A., Bai, X., Fu, C., Zhang, R., Campbell, F., Liao, X., Coller, J., and Jain, M.K. (2015a). KLF15 establishes the landscape of diurnal expression in the heart. Cell Rep. *13*, 2368–2375.

Zhang, R., Lahens, N.F., Ballance, H.I., Hughes, M.E., and Hogenesch, J.B. (2014). A circadian gene expression atlas in mammals: implications for biology and medicine. Proc. Natl. Acad. Sci. U S A *111*, 16219–16224.

Zhang, R., Podtelezhnikov, A.A., Hogenesch, J.B., and Anafi, R.C. (2016). Discovering biology in periodic data through phase set enrichment analysis (PSEA). J. Biol. Rhythms *31*, 244–257.

Zhang, Y., Fang, B., Emmett, M.J., Damle, M., Sun, Z., Feng, D., Armour, S.M., Remsberg, J.R., Jager, J., Soccio, R.E., et al. (2015b). Discrete functions of nuclear receptor Rev-erb couple metabolism to the clock. Science *348*, 1488–1492.

Zhang, Z., Xin, H., and Li, M.-D. (2020b). Circadian rhythm of lipid metabolism in health and disease. Small Methods *4*, 1900601.

iScience, Volume *24*

Supplemental information

A multi-tissue multi-omics analysis reveals distinct kineztics in entrainment of diurnal transcriptomes by inverted feeding

Haoran Xin, Fang Deng, Meiyu Zhou, Rongfeng Huang, Xiaogen Ma, He Tian, Yan Tan, Xinghua Chen, Dan Deng, Guanghou Shui, Zhihui Zhang, and Min-Dian Li

Supplemental Documents

Supplemental Figure 1

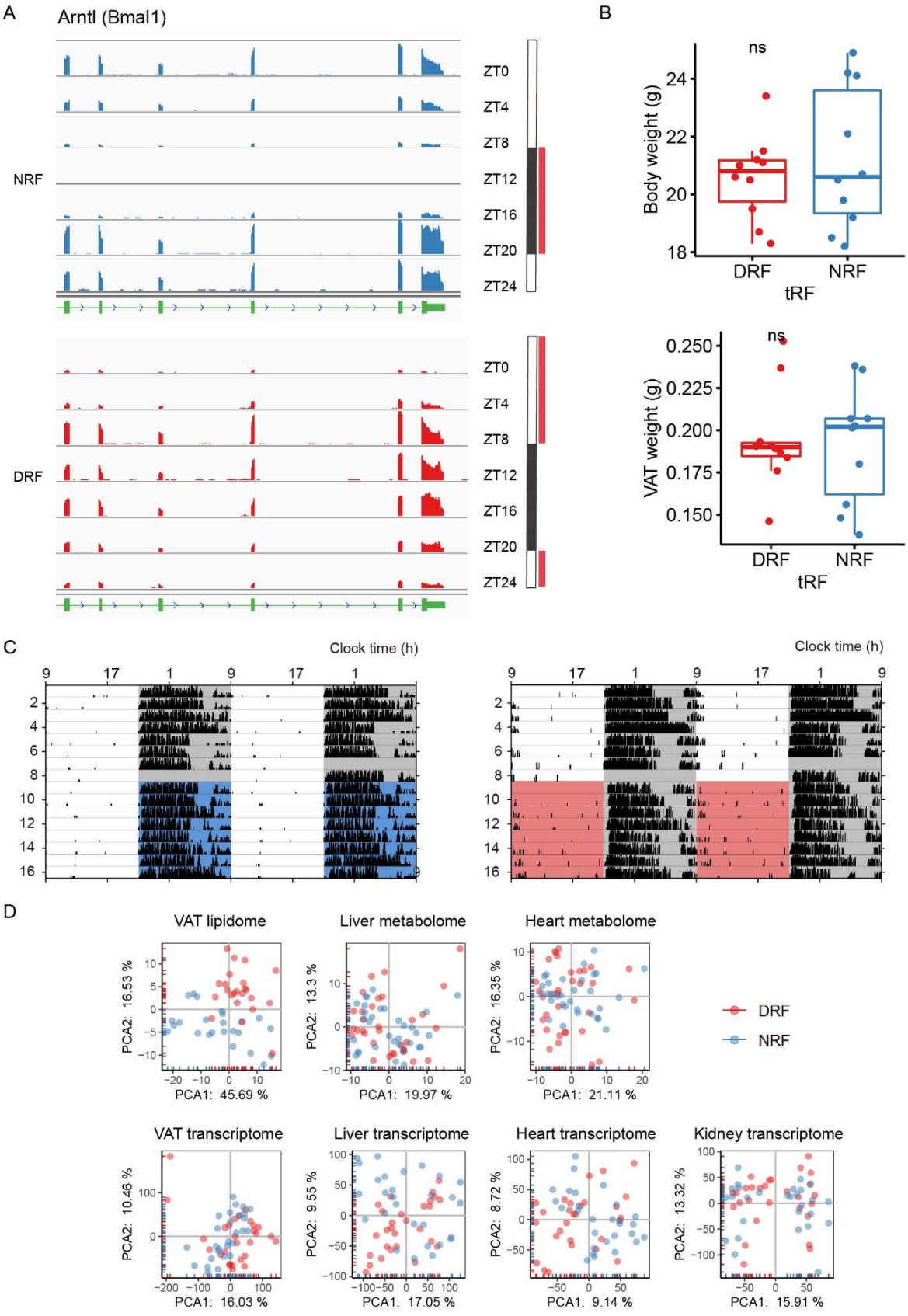

Figure S1, Related to Figure 1.

(A) Read counts from the clock output gene *Arntl* locus exhibit diurnal rhythms in liver.

(B) Records of diurnal body weight and visceral adipose tissue (VAT) weight of 9 weeks old female mice that had been on DRF or NRF for 1 week (n = 10). Data are represented in boxplots as a five-number summary, i.e. minimum, first quartile, median, third quartile, and maximum. Wilcoxon tests, $P >= 0.05$, ns, not significant.

(C) Wheel-running activity recordings of female mice under NRF (blue shade) and DRF (red shade). Blue/red shades indicate time of feeding. Horizontal axis indicates clock time in 24 hours. Vertical axis indicates days after the recording began. Representative actograms are shown.

(D) Principal component analysis of diurnal transcriptomes and metabolomes in peripheral tissues subjected to tRF regimens. Eigen value is indicated after PCA1 and PCA2.

Supplemental Figure 2

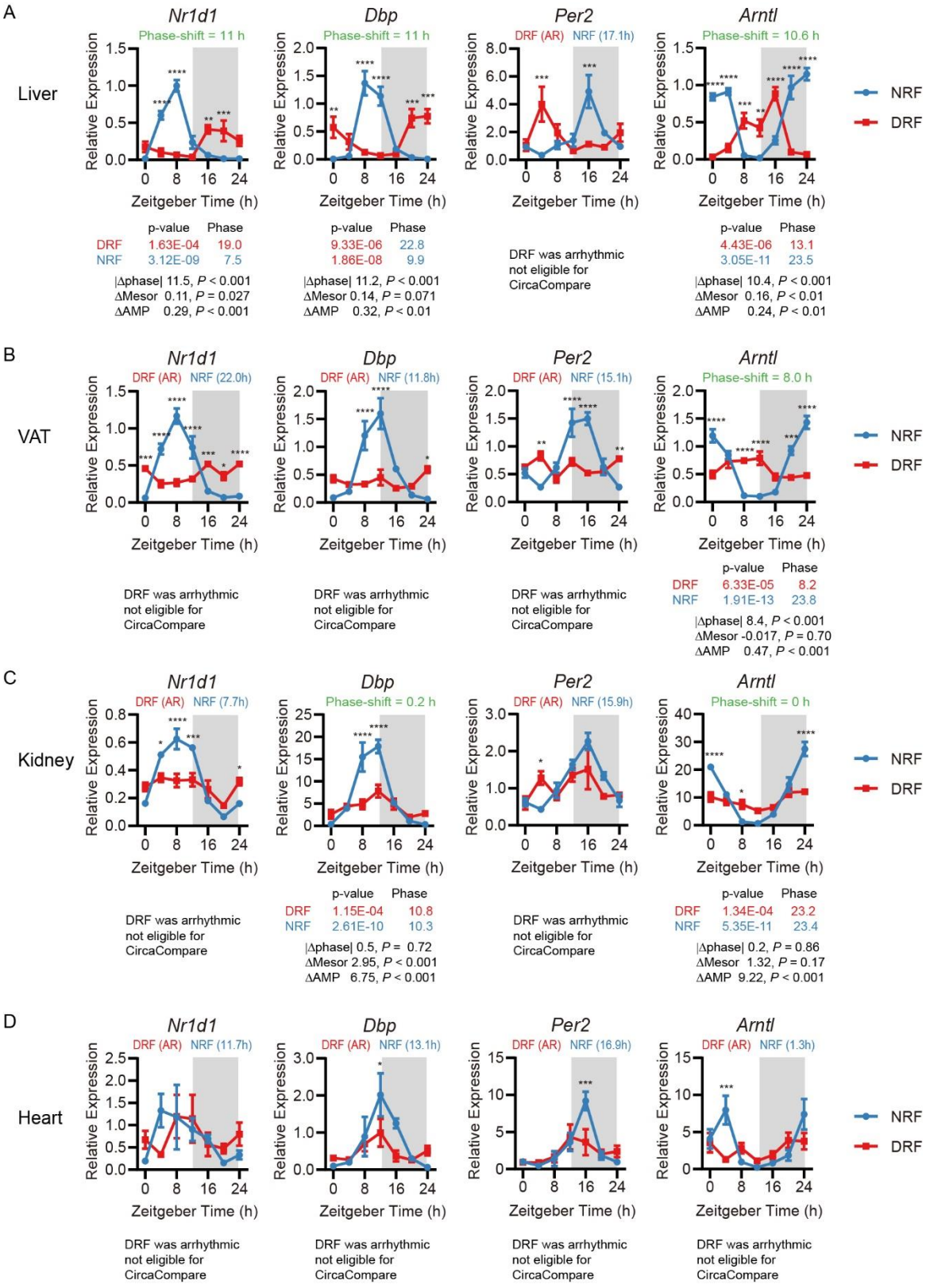

Figure S2. Clock Entrainment by Inverted Feeding in Male Mice, Related to Figure 2. (A-D) Diurnal expression of clock genes in liver (**A**), VAT (**B**), kidney (**C**), and heart (**D**). C57BL/6J male mice at the age of 7 weeks were acclimated to 12/12h light/dark cycle for one

week, and subjected to tRF regimens for 7 days. Data are represented as mean ± sem (n = 4, except n = 3 in kidney ZT0 group). Multiple t-tests with Bonferroni correction; not shown when $P >= 0.05$, *$P < 0.05$, ** $P < 0.01$, *** $P < 0.001$. Circadian rhythmicity parameters were determined by MetaCycle (presented at the top of graphs) and CircaCompare (presented at the bottom of graphs) with the period set to 24 h. Phase shift is represented in absolute value. AR, arrhythmic; mesor, rhythm-adjusted mean expression level; AMP, amplitude.

Supplemental Figure 3

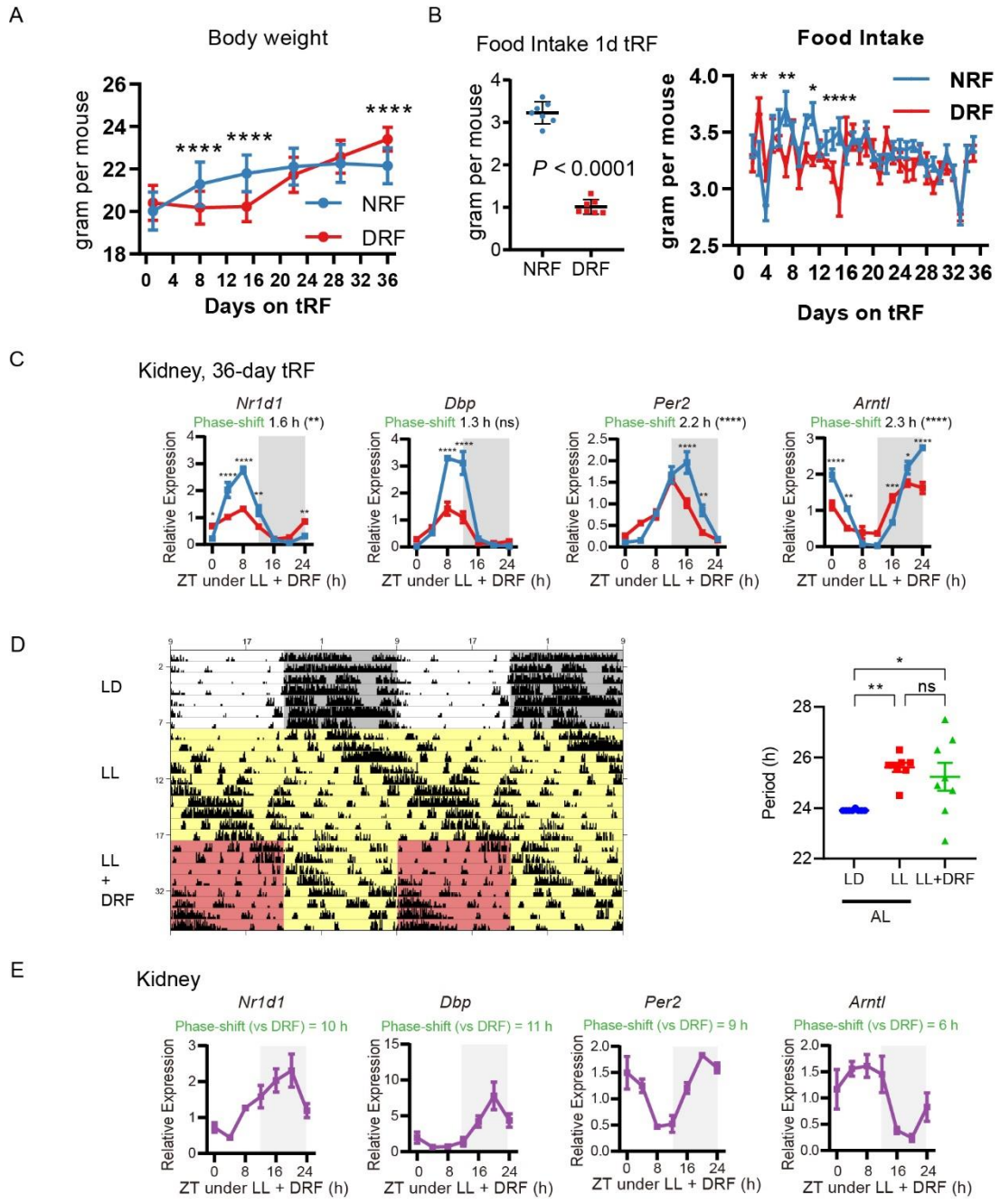

Figure S3. Effects of Duration and Constant Light on Clock Entrainment by Inverted Feeding, Related to Figure 3.

(A) Weekly monitoring of body weight from female mice on DRF or NRF. Data are represented as mean ± sd (n = 28). Multiple t-tests with Bonferroni correction; not shown when $P >= 0.05$, **** $P < 0.0001$.

(B) Daily monitoring of food intake from female mice on DRF or NRF. Data are represented as mean ± sd (n = 28 in total, average of food consumption from 7 cages containing 4 mice) for Day 1 and mean ± sem for other time-points. 1d tRF, Day 1 on time-restricted feeding. Student's t-test or multiple t-tests with Bonferroni correction; not shown when $P >= 0.05$, *$P < 0.05$, ** $P < 0.01$, *** $P < 0.001$, **** $P < 0.0001$.

(C) Effects of 36-day inverted feeding on diurnal expression of clock genes in kidney. Phase-shifts were computed by CircaCompare. t-tests provided by CircaCompare or multiple t-tests with Bonferroni correction; ns or not shown when $P >= 0.05$, *$P < 0.05$, ** $P < 0.01$, *** $P < 0.001$, **** $P < 0.0001$.

(D) Wheel-running activity recordings and statistics of female mice under normal light/dark cycle (LD), constant light (LL, yellow shade) and LL+DRF (red/yellow shade). Red indicates feeding time. Horizontal axis indicates clock time in 24 hours. Vertical axis indicates days after the recording began. A representative actogram is shown. Data are represented as mean ± sem (n = 8). 1-way ANOVA with Bonferroni correction; ns, not significant when $P >= 0.05$, *$P < 0.05$, ** $P < 0.01$.

(E) Effects of constant light (LL) on diurnal expression of clock genes in kidney under DRF. Female mice were acclimated to 12h light-dark cycles, subjected to LL for 9 days, and then subjected to DRF and constant lightness for 7 days. Phase shift was estimated by meta2d_phase (h) with the period length under LL set to 20-28h and that under LD set to 24h. CircaCompare could not be applied because the period length under LL differs significantly from that under 12h light-dark cycles. DRF, daytime-restricted feeding; NRF, nighttime-restricted feeding. Data are represented as mean ± sem (n = 4). Multiple t-tests with Bonferroni correction; not shown when $P >= 0.05$, *$P < 0.05$, ** $P < 0.01$, *** $P < 0.001$.

Supplemental Figure 4

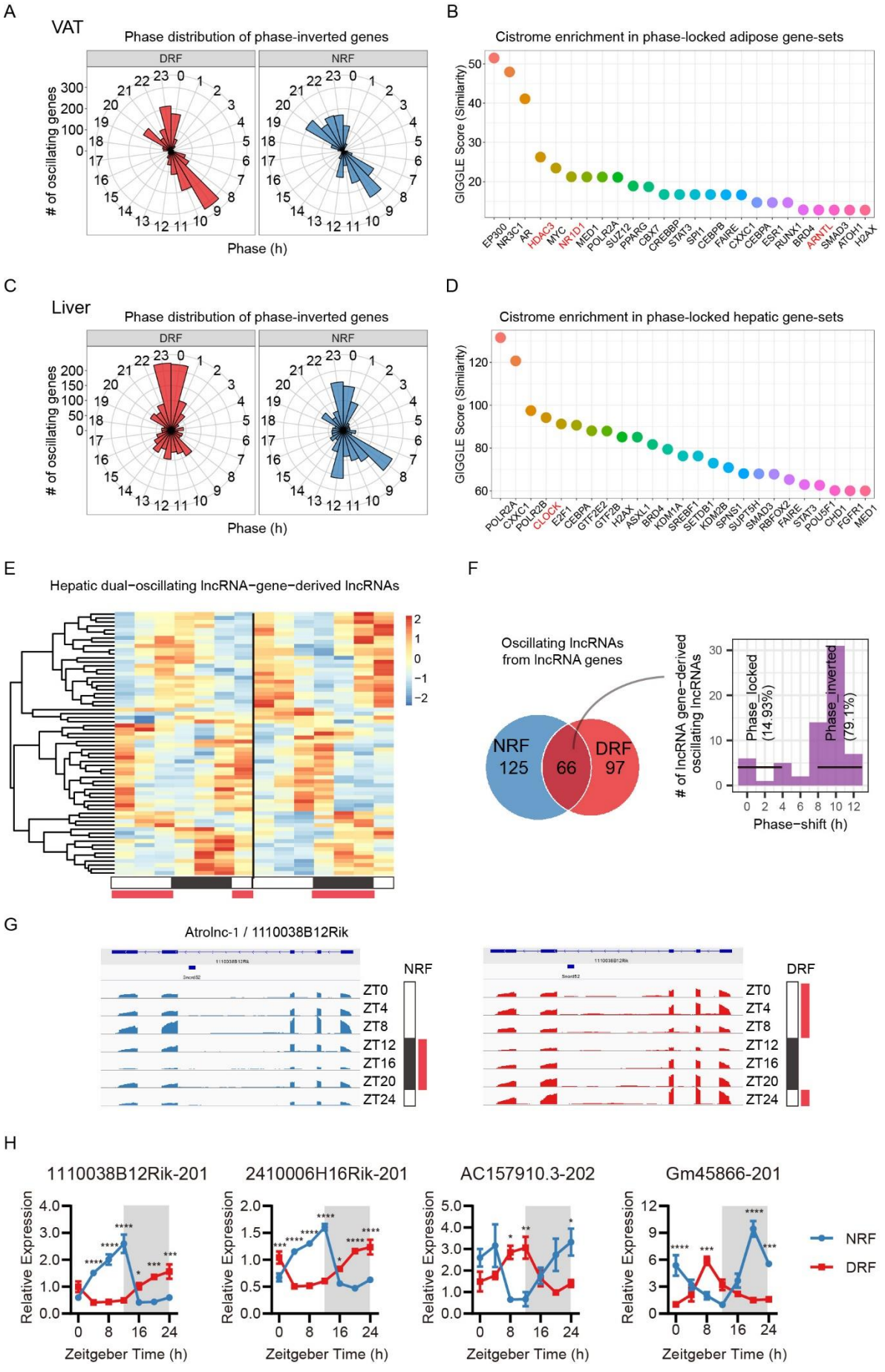

Figure S4. Circadian and Phase Analysis of Diurnal Transcriptomes in VAT and Liver, Related to Figure 4.

(A) Phase distribution of phase-inverted genes in VAT.

(B) Cistrome enrichment analysis of phase-locked genes in VAT based on curated hepatic cistromes of transcription factors and chromatin regulators from CistromeDB.

(C) Phase distribution of phase-inverted genes in liver.

(D) Cistrome enrichment analysis of phase-locked genes in liver based on curated hepatic cistromes of transcription factors and chromatin regulators from CistromeDB.

(E) Heatmap showing 24 h expression profiles of dual-oscillating lncRNA-gene-derived lncRNA transcripts in liver.

(F) 79.1% of the 66 oscillating lncRNAs from lncRNA genes in liver are phase-inverted by inverted feeding.

(G) Diurnal profiles of read counts of 1110038B12Bik (Atrolnc-1) lncRNA.

(F) 24h expression profiles of selected dual-oscillating lncRNA gene-derived lncRNAs. Data are represented as mean ± sem (n = 4). Multiple t-tests with Bonferroni correction; not shown when $P >= 0.05$, *$P < 0.05$, ** $P < 0.01$, *** $P < 0.001$, **** $P < 0.0001$.

Supplemental Figure 5

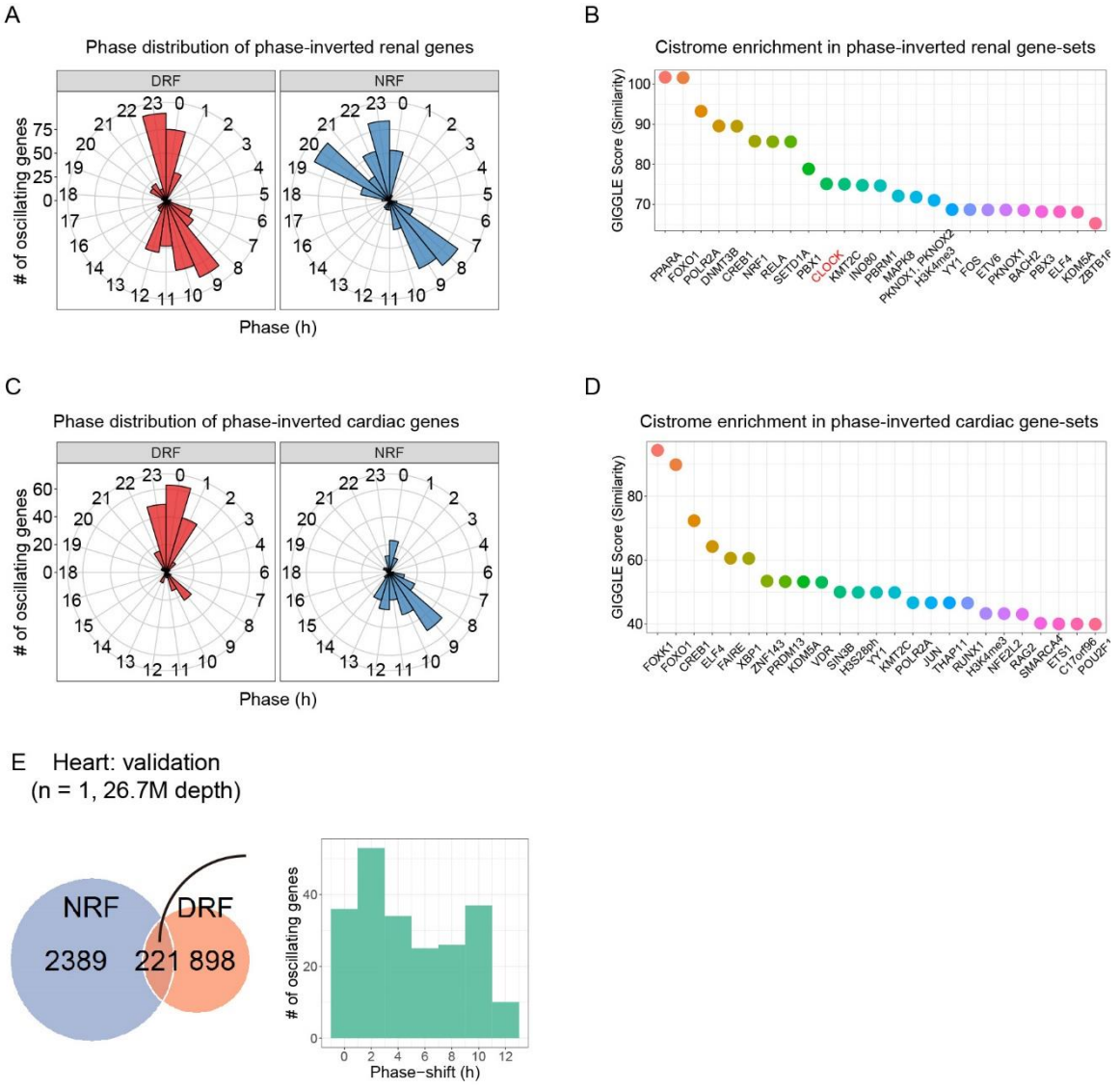

Figure S5. Circadian and Phase Analysis of Diurnal Transcriptomes in Kidney and Heart, Related to Figure 5.

(A) Phase distribution of phase-inverted genes in kidney.

(B) Cistrome enrichment analysis of phase-inverted genes in kidney based on curated hepatic cistromes of transcription factors and chromatin regulators from CistromeDB.

(C) Phase distribution of phase-inverted genes in heart.

(D) Cistrome enrichment analysis of phase-inverted genes in heart based on curated hepatic cistromes of transcription factors and chromatin regulators from CistromeDB.

(E) General feature of a validation cohort testing phase entrainment of cardiac diurnal transcriptome by feeding. RNA-seq data depth is at least 26.7 million reads. Rhythmicity is defined as meta2d_pvalue < 0.1, period is set to 24 h.

Supplemental Figure 6

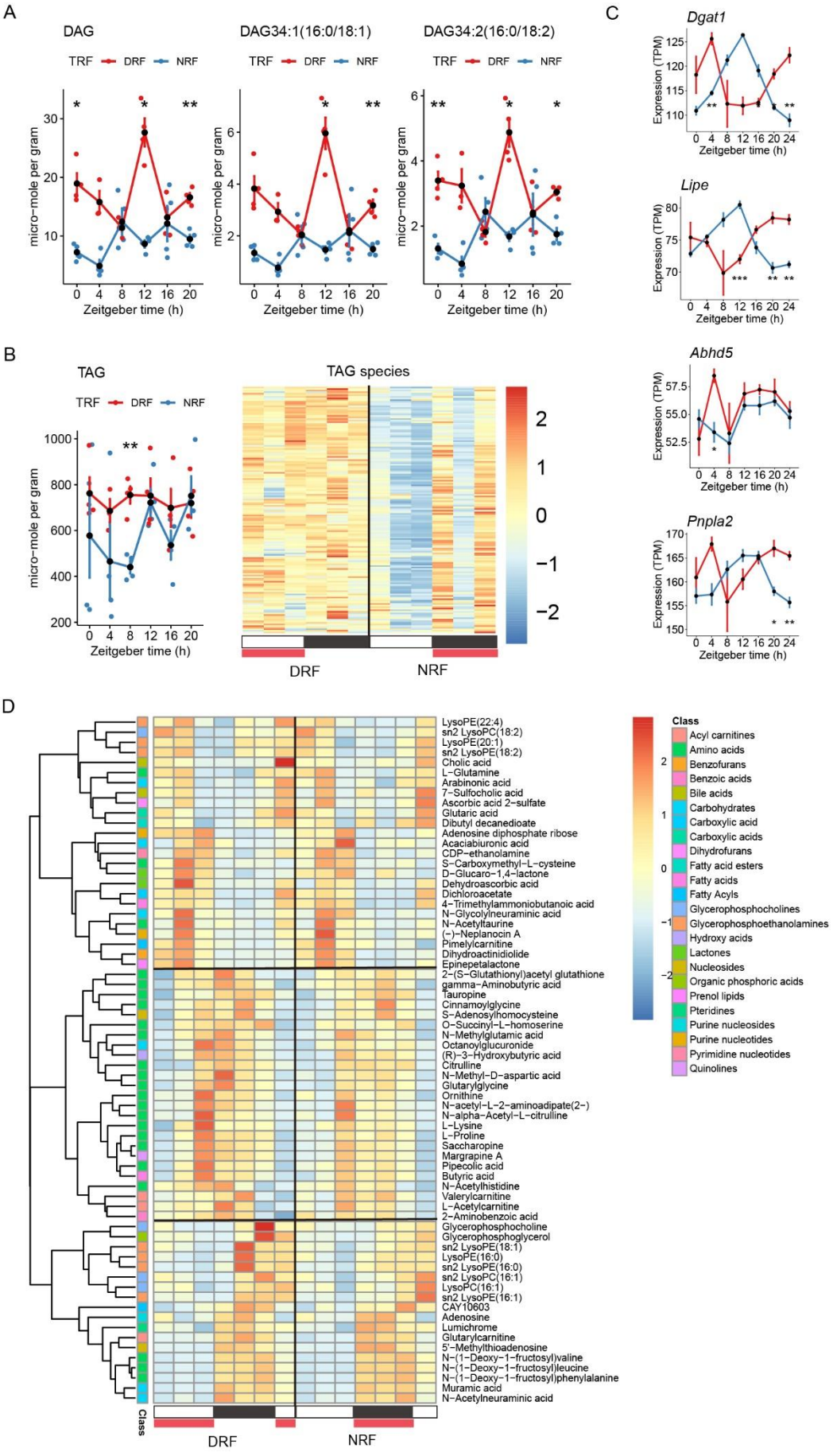

Figure S6. Circadian and Phase Analysis of Adipose Lipidome and Hepatic Metabolome, Related to Figure 6.

(A) Diurnal profiles of major diacylglycerol (DAG) species in adipose tissue. Data were represented as mean ± sem (n = 4 except n = 3 in DRF ZT4 group). Multiple t-tests with Bonferroni correction; *P* >= 0.05 is not shown; **P* < 0.05; ***P* < 0.01.

(B) Heatmap showing diurnal profiles of triacylglycerols (TAG) in adipose tissue. ROUT outlier analysis was performed for total TAG levels, but no outlier was identified at a threshold Q of 0.01. Data were represented as mean ± sem (n = 4 except n = 3 in DRF ZT4 group). Multiple t-tests with Bonferroni correction; *P* >= 0.05 is not shown; ***P* < 0.01.

(C) Diurnal expression profiles of genes involved in DAG/TAG metabolism. Data were represented as mean ± sem (n = 4). Multiple t-tests with Bonferroni correction; *P* >= 0.05 is not shown; **P* < 0.05; ***P* < 0.01, ****P* < 0.001.

(D) 24 h profiles of hepatic metabolites that oscillate under at least one tRF regimen.

Supplemental Figure 7

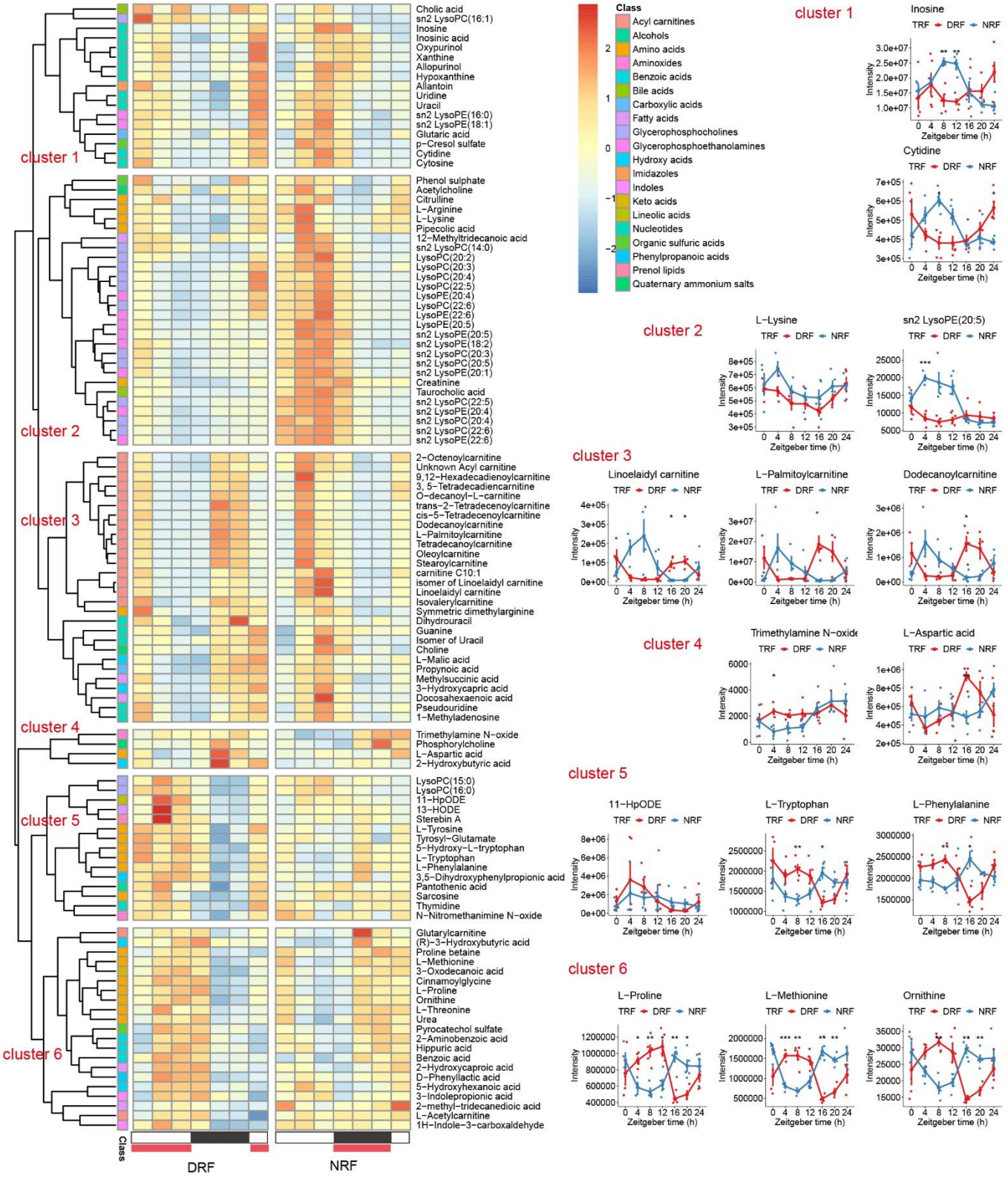

Figure S7. Circadian and Phase Analysis of Cardiac Metabolomes, Related to Figure 7.
Heatmap showing diurnal profiles of diurnal metabolites in heart. Euclidean clustering grouped cardiac diurnal metabolites into six clusters. Diurnal profiles of representative

metabolites from the five clusters were shown as mean ± sem (n = 4-5). Multiple t-tests with Bonferroni correction; $P >= 0.05$ is not shown; *$P < 0.05$; **$P < 0.01$, ***$P < 0.001$.

Supplemental Table 6

Oligonucleotides	SOURCE
Primers: Arntl Forward: CTTGCAAGCACCTTCCTTCC Reverse: GGGTCATCTTTGTCTGTGTC	This paper
Primers: Per2 Forward: ATGCTCGCCATCCACAAGA Reverse: GCGGAATCGAATGGGAGAAT	This paper
Primers: Nr1d1 Forward: TACATTGGCTCTAGTGGCTCC Reverse: CAGTAGGTGATGGTGGGAAGTA	This paper
Primers: Dbp Forward: CGTGGAGGTGCTAATGACCTTT Reverse: CATGGCCTGGAATGCTTGA	This paper
Primers: u36B4 Forward: AGATGCAGCAGATCCGCAT Reverse: GTTCTTGCCCATCAGCACC	This paper
Primers: 1110038B12Rik-201 Forward: GCACAATGGGATTTGAGGACAC Reverse: GACAAAGGGCTGGCTCTCAT	This paper
Primers: 2410006H16Rik-201 Forward: TGCTCTTCTCGCTCGTTGAG Reverse: TTGTCAACGTCCCGTCAGG	This paper
Primers: AC157910.3-202 Forward: GTGACTCTGTTCCCTGGTGA Reverse: TGTGGAGTCACTTTGCTGCA	This paper
Primers: Gm45866-201 Forward: AAACAGCCACCACACGGTAC Reverse: CCCTTCCAGTTGGCCTTTGA	This paper

Table S6. RT-qPCR Primers Used for Circadian Rhythm Validation, Related to Figure 2, Figure 3, and Figure 4

Transparent Methods

EXPERIMENTAL MODEL AND SUBJECT DETAILS

Animals

Animal experiments were approved by the Laboratory Animal Welfare and Ethics Committee of the Third Military Medical University (TMMU), China. All experiments conform to the relevant regulatory standards of TMMU. Special pathogen-free (SPF) mice were purchased from Hunan SJT Laboratory Animal Co. and housed in a SPF barrier facility. C57BL/6J female or male mice at 6 or 7 weeks of age were grouped housed, and entrained to a 12h light:12h dark cycle with normal chow food and water *ad libitum* during acclimation for at least one week. Animals were randomly assigned in a 1:1 ratio to time-restricted feeding groups. The body weight statistics were balanced between groups before subjected to time-restricted feeding.

METHOD DETAILS

Time-restricted feeding and sample collection

For transcriptome and metabolome profiling

C57BL/6J female mice at 7 weeks of age were grouped housed, and entrained to a 12h light:12h dark cycle (light intensity 200 lux) with normal chow food and water *ad libitum* for at least 7 days before assigned to daytime-restricted feeding (DRF) and nighttime-restricted feeding (NRF) groups for 7 days. The DRF group had access to food for 12 h from ZT0 to ZT12 where ZT0 denotes light on at 9:00 am in China Standard Time (UTC +8). The NRF group had access to food for 12 h from ZT12 to ZT24 (ZT0). At the end of time-restricted feeding, mice were euthanized by cervical dislocation, and subjected to tissue collection every 4 h over 24 h. Visceral adipose tissue, liver, and heart were collected from one batch (n = 4 per group per time-point). Liver and heart were collected from a second batch for metabolomics (n = 5 per group per time-point; liver samples D24_5 and N24_5 could not be identified because of incorrect labels). Kidney were collected from a third batch (n = 4 per group per time-point). Visceral adipose tissue were collected for lipidomics analysis (n = 4 per group per time-point). Tissues were snap frozen in liquid nitrogen and stored in a -80 deg fridge.

Clock entrainment to inverted feeding in male mice

C57BL/6J male mice at 7 weeks of age were grouped housed, and entrained to a 12h light:12h dark cycle (light intensity 500 lux for male, this is within the range of normal indoor illumination) with normal chow food and water *ad libitum* for at least 7 days before assigned to daytime-restricted feeding (DRF) and nighttime-restricted feeding (NRF) groups for 7 days. The DRF group had access to food for 12 h from ZT0 to ZT12 where ZT0 denotes light on at 9:00 am in China Standard Time (UTC +8). The NRF group had access to food for 12 h from ZT12 to ZT24 (ZT0). At the end of time-restricted feeding, mice were euthanized by cervical dislocation, and subjected to tissue collection every 4 h over 24 h. Visceral adipose tissue, liver, kidney and heart were collected (n = 4 per group per time-point). Tissues were snap frozen in liquid nitrogen and stored in a -80 deg fridge.

Long-term regimens of time-restricted feeding

C57BL/6J female mice at 7 weeks of age were grouped housed, and entrained to a 12h

light:12h dark cycle (light intensity 200 lux) with normal chow food and water *ad libitum* for at least 7 days before assigned to daytime-restricted feeding (DRF) and nighttime-restricted feeding (NRF) groups for 36 days. The DRF group had access to food for 12 h from ZT0 to ZT12 where ZT0 denotes light on at 9:00 am in China Standard Time (UTC +8). The NRF group had access to food for 12 h from ZT12 to ZT24 (ZT0). At the end of time-restricted feeding, mice were euthanized by cervical dislocation, and subjected to tissue collection every 4 h over 24 h. Visceral adipose tissue, liver, kidney and heart were collected (n = 4 per group per time-point). Tissues were snap frozen in liquid nitrogen and stored in a -80 deg fridge.

Constant light exposure

Six-week old C57BL/6J female mice were group-housed, acclimated (light intensity 500 lux) for 7 days, exposed to constant light (LL) for 9 days to induce behavioral arrhythmia (Chen et al., 2008), and subjected to DRF and LL for 9 days. At the end of time-restricted feeding, mice were euthanized by cervical dislocation, and subjected to tissue collection every 4 h over 24 h. Visceral adipose tissue, liver, kidney and heart were collected (n = 4 per group per time-point). Tissues were snap frozen in liquid nitrogen and stored in a -80 deg fridge.

Food intake, body weight, and locomotor activity analyses

Mice were housed in groups (n = 4 per cage, n = 7 cages per treatment) and ear-tagged. Body weight was monitored weekly by a digital precision scale (accuracy 0.1 g) for 36 days. Food intake per cage was manually weighed by a digital precision scale (accuracy 0.1 g) on a daily basis for 36 days. Food pellets were layed on the bedding of cages to avoid smashing and weighed 48 h later. Food intake was represented as food consumption per day per mouse (food consumed in grams divided by (2 days x 4 mice per cage)). For locomotor activity analysis, mice were individually housed and acclimated in 12 h light/dark cycle for two weeks in a cage with a running wheel. Wheel running was recorded in 1-min bins and analyzed using ClockLab (Actimetrics, Evanston, IL). Locomotor actograms were double-plotted.

Global Profiling of Transcripts

Strand-specific sequencing of cDNA library from liver

Total RNA was extracted by TRIzol method (Invitrogen). RNA integrity, purity and concentration were assessed by RNA electrophoresis, the NanoPhotometer spectrophotometer, and the Bioanalyzer 2100 system (Thermo Fisher Scientific, MA, USA). All RNA samples passed the quality control. About 100 mg of liver was subjected to homogenization. One sample represents one mouse and four biological replicates were set up for each time point per dietary treatment. In total, there were 56 RNA extractions for preparing hepatic strand-specific cDNA library.

Library construction, RNA sequencing, read mapping, and gene/transcript quantification were performed by Novogene (Beijing, China). A ribosome-depletion workflow was applied to generate the strand-specific cDNA library (Parkhomchuk et al., 2009). Specifically, ribosomal RNAs were removed by Epicenter Ribo-Zero Kit (Epicenter). The remaining RNAs were fragmented (250-300 bp), and reversely transcribed using random hexamers and M-MuLV Reverse Transcriptase (RNase H-). After RNA digestion by RNase H, second strand cDNA synthesis was subsequently performed using dNTP (dTTP replaced by dUTP) and DNA

polymerase I, followed by purification, terminal repair, polyadenylation, adapter ligation, size selection, and degradation of second-strand U-contained cDNA. The clustering of the index-coded samples was performed on a cBot Cluster Generation System using TruSeq PE Cluster Kit v3-cBot-HS (Illumina) according to the manufacturer's instructions. After cluster generation, the library preparations were sequenced on an Illumina Novaseq6000 platform and 150 bp paired-end reads (PE150) were generated. About 10% of the ribosome-depleted transcript profile contains circular RNA (circRNA), which permits to explore diurnal oscillation of circRNAs.

RNA sequencing of cDNA library from VAT and heart

Total RNA was extracted by TRIzol method (Invitrogen). RNA integrity, purity and concentration were assessed by RNA electrophoresis, the NanoPhotometer spectrophotometer, and the Bioanalyzer 2100 system (Thermo Fisher Scientific, MA, USA). All RNA samples passed the quality control. Two lobes of VAT, or the whole heart were subjected to homogenization. One sample represents one mouse and four biological replicates were set up for each time point per dietary treatment. In total, there were 56 RNA extractions for preparing cDNA libraries of visceral adipose or cardiac mRNAs.

Library construction, RNA sequencing, read mapping, and gene/transcript quantification were performed by Novogene (Beijing, China). A total amount of 1 μg RNA per sample was used as input material for the RNA sample preparations. Sequencing libraries were generated using NEBNext® Ultra RNA Library Prep Kit for Illumina (NEB, USA) following manufacturer's recommendations and index codes were added to attribute sequences to each sample. Briefly, mRNA was purified from total RNA using poly-T oligo-attached magnetic beads. Fragmentation was carried out using divalent cations under elevated temperature in NEBNext First Strand Synthesis Reaction Buffer(5X). First strand cDNA was synthesized using random hexamer primer and M-MuLV Reverse Transcriptase (RNase H-). Second strand cDNA synthesis was subsequently performed using DNA Polymerase I and RNase H. Remaining overhangs were converted into blunt ends via exonuclease/polymerase activities. After adenylation of 3' ends of DNA fragments, NEBNext Adaptor with hairpin loop structure were ligated to prepare for hybridization.

In order to select cDNA fragments of preferentially 250~300 bp in length, the library fragments were purified with AMPure XP system (Beckman Coulter, Beverly, USA). Then 3 μl USER Enzyme (NEB, USA) was used with size-selected, adaptor-ligated cDNA at 37°C for 15 min in followed by 5 min at 95 °C before PCR. Then PCR was performed with Phusion High-Fidelity DNA polymerase, Universal PCR primers and Index (X) Primer. At last, PCR products were purified (AMPure XP system) and library quality was assessed on the Agilent Bioanalyzer 2100 system. The clustering of the index-coded samples was performed on a cBot Cluster Generation System using TruSeq PE Cluster Kit v3-cBot-HS (Illumina) according to the manufacturer's instructions. After cluster generation, the library preparations were sequenced on an Illumina Novaseq6000 platform and 150 bp paired-end reads (PE150) were generated.

RNA sequencing of cDNA library from heart (for validation)

Library construction, RNA sequencing, read mapping, and gene/transcript quantification were performed by Biomarker Technologies (Beijing, China). All RNA samples passed the quality control. Whole heart was subjected to homogenization. As a small-scale validation

experiment, heart samples were collected from a different batch of animals of same age, sex, and treatment, except one mouse was assigned per time point. One sample represents one mouse. In total, there were 14 RNA extractions for preparing cDNA libraries of cardiac mRNAs. Total RNAs were extracted by TRIzol method (Invitrogen). RNA concentration/purity and integrity was measured by NanoDrop 2000 (Thermo Fisher Scientific, Wilmington,DE) and the RNA Nano 6000 Assay Kit of the Agilent Bioanalyzer 2100 system (Agilent Technologies, CA, USA). 1 μg RNA per sample was used for library construction. Sequencing libraries were prepared as described in the previous section. The clustering of the index-coded samples was performed on a cBot Cluster Generation System using TruSeq PE Cluster Kit v4-cBot-HS (Illumina) according to the manufacturer's instructions. After cluster generation, the library preparations were sequenced on an Illumina's Novaseq6000 platform and PE150 reads were generated.

RNA sequencing of cDNA library from kidney

Total RNA was extracted by TRIzol method (Invitrogen). RNA integrity, purity and concentration were assessed by RNA electrophoresis, NanoDrop, and the Bioanalyzer 2100 system (Thermo Fisher Scientific, MA, USA). All RNA samples passed the quality control. The left lobe of kidney was subjected to homogenization. One sample represents one mouse and four biological replicates were set up for each time point per dietary treatment. In total, there were 56 RNA extractions for preparing cDNA libraries of renal mRNAs.

Library construction, RNA sequencing, read mapping, and gene/transcript quantification were performed by BGI (Beijing, China). Oligo(dT)-attached magnetic beads were used to purified mRNA. Purified mRNA was fragmented into small pieces with fragment buffer at an appropriate temperature. Then First-strand cDNA was generated using random hexamer-primed reverse transcription, followed by a second-strand cDNA synthesis. Afterwards, A-Tailing Mix and RNA Index Adapters were added by incubating to end repair. The cDNA fragments obtained from previous step were amplified by PCR, and products were purified by Ampure XP Beads, then dissolved in EB solution. The product was validated on the Agilent Technologies 2100 bioanalyzer for quality control. The double stranded PCR products from previous step were heated denatured and circularized by the splint oligo sequence to get the final library. The single strand circle DNA (ssCir DNA) was formatted as the final library. The final library was amplified with phi29 to make DNA nanoball (DNB) which had more than 300 copies of one molecule. DNBs were loaded into the patterned nanoarray and pair end 150 bases reads (PE150) were generated on BGIseq500 platform (BGI-Shenzhen, China).

Untargeted metabolomics

The extraction protocol for sample metabolome were referenced to a previous method (Yuan et al., 2012). Chromatographic separation was performed on a reversed-phase ACQUITY UPLC HSS T3 1.8 μm, 3.0 × 100 mm columns (Waters, Dublin, Ireland) using an ultra-performance LC system (Agilent 1290 Infinity II; Agilent Technologies, Germany). MS was performed using high-resolution mass spectrometry (5600 Triple TOF Plus, AB Sciex, Singapore) equipped with an ESI source. Data were acquired in TOF full scan method with positive and negative ion modes, respectively. Information-dependent acquisition methods were used for MS/MS analyses of metabolome. The collision energy was set at 35 ± 15 eV.

Metabolite identification was compared with standard references, HMDB (http://www.hmdb.ca/) and METLIN (https://metlin.scripps.edu). 45 isotopically-labeled internal standards were spiked into the samples for semi-quantification of metabolites (see Key Resources Table in Mendeley Data).

Metabolite intensities were normalized according to the following rules, and referred to as Intensity (Song et al., 2020). (1) Peak areas of metabolites were counted when internal standards were available; (2) When Step (1) was not feasible due to unavailability of commercial standards, peak areas were corrected with IS of metabolites of the same class, comparable peak intensities, and/or proximity in retention times; (3) Results from Step (2) were evaluated based on relative standard deviation (RSD) values of each metabolite before and after IS correction. Corrected peak areas were adopted if their corresponding RSDs were smaller than that of original areas in quality control samples.

Targeted lipidomics

Lipid extracts from adipose tissue were prepared by a modified Bligh/Dyer method and analyzed (Lu et al., 2019). Samples were resuspended and spiked with appropriate concentrations of isotope-labeled internal standards. All lipidomics analyses were conducted on an Exion UPLC coupled with a SCIEX QTRAP 6500 PLUS system in an ESI mode (curtain gas = 20, ion spray voltage = 5500 V, temperature = 400 degrees, ion source gas 1 = 35, ion source gas 2 = 35). Glycerolipids including diacylglycerols (DAGs) and triacylglycerols (TAGs) were quantified using a modified version of reverse phase LC/MRM. Separation of neutral lipids were achieved on a Phenomenex Kinetex-C18 2.6 µm column (i.d. 4.6x100 mm) using an isocratic mobile phase containing chloroform:methanol:0.1 M ammonium acetate 100:100:4 (v/v/v) at a flow rate of 160 µL/min. Levels of TAGs were estimated by referencing to spiked internal standards of TAG(14:0)3-d5, TAG(16:0)3-d5 and TAG(18:0)3-d5 obtained from CDN isotopes (Quebec, Canada), respectively. DAGs were quantified using d5-DAG(1,3-17:0) and d5-DAG(1,3-18:1) as internal standards from Avanti Polar Lipids. Free cholesterol and cholesteryl esters were analyzed by HPLC-MS/MS in an APCI mode, and estimated by referencing to internal standards, i.e. cholesterol-26,26,26,27,27,27-d6 and cholesteryl-2,2,3,4,4,6-d6 Octadeconate (CDN isotopes). Lipid levels were expressed in nanomole or micromole of lipids per gram of wet tissue.

Acyl-CoA quantification by LC/MS

Extraction of acyl-CoAs from heart tissue was carried out as follows (Woldegiorgis et al., 1985). 300 µL of extraction buffer containing isopropanol, 50 mM KH2PO4, 50 mg/mL BSA (25:25:1 v/v/v) acidified with glacial acetic acid was added to cells. Next, 19:0-CoA was added as an internal standard and lipids were extracted by incubation at 4 °C for 1 h at 1500 rpm. Following this, 300 µL of petroleum ether was added and the sample was centrifuged at 12,000 rpm for 2 min at 4 °C. The upper phase was removed. The samples were extracted two more times with petroleum ether as described above. To the lower phase finally remaining, 5 µL of saturated ammonium sulfate was added followed by 600 µL of chloroform:methanol (1:2 v/v). The sample was then incubated on a thermomixer at 450 rpm for 20 min at 25 °C, followed by centrifugation at 12000 rpm for 5 min at 4 °C. Clean supernatant was transferred to fresh tube and subsequently dried in the SpeedVac under OH mode (Genevac). Dry extracts were

resuspended in appropriate volume of methanol:water (9:1 v/v) prior to liquid chromatography–mass spectrometry (LC–MS) analyses on a Thermofisher U3000 DGLC coupled to Sciex QTRAP 6500 Plus (Lam et al., 2020).

RNA extraction and real-time quantitative PCR

Tissue RNAs were isolated using Eastep® Super Total RNA Extraction Kit (Promega). Complementary DNA (cDNA) was synthesized using the GoScript™ Reverse Transcription Mix (Promega). cDNA was amplified and analyzed using iTaq™ universal SYBR ® Green Supermix (Bio-Rad) and the Bio-Rad CFX96 Real-Time PCR Detection System (Bio-Rad). PCR protocol: Polymerase activation and DNA denaturation at 95 degrees for 3 min; denaturation at 95 degrees for 10 sec; annealing/extension and plate read at 60 degrees for 30 sec; 40 cycles of quantitative PCR. Results were normalized to u36b4. Primer sequences were listed in Key Resource Table. Experiments were repeated at least twice.

QUANTIFICATION AND STATISTICAL ANALYSIS

Bioinformatics for global transcript profiling

Strand-specific sequencing of cDNA library from liver

Raw data (raw reads) of fastq format were firstly processed through in-house perl scripts (Novogene). In this step, clean data (clean reads) were obtained by removing reads containing adapter, reads containing ploy-N and low-quality reads from raw data. At the same time, Q20, Q30 and GC content the clean data were calculated. All the downstream analyses were based on the clean data with high quality. Reference genome and gene model annotation files were downloaded from genome website directly. HISAT2 v2.0.5 (Kim et al., 2015) was used to index the reference genome (mus_musculus_Ensembl_97) and map the paired-end clean reads. using HISAT2 v2.0.5. Transcripts were assembled by StringTie (Pertea et al., 2015), and determined by Cuffmerge, which filters undirectional and short (< 200 nt) transcripts (Trapnell et al., 2012). Noval lncRNA and mRNAs were determined by Cuffcompare (Trapnell et al., 2012). Particularly, novel lncRNA was determined by their lack of annotation in the current database, and lack of protein-coding potential using CPC2, PFAM, CNCI. Transcript/gene read counts were quantified by StringTie (Pertea et al., 2015). The read counts were normalized by TMM (Trimmed Mean of M-values) method by edgeR (v3.30.3) (Robinson et al., 2010), and converted to Wagner's TPM (Transcripts per Million), based on the length of the gene and reads count mapped to a gene (Wagner et al., 2012). Gene/transcripts with TPM > 1 in at least 20% samples were considered as robustly expressed and kept for downstream analysis.

RNA sequencing of cDNA library from VAT and heart

Raw data (raw reads) of fastq format were firstly processed through in-house perl scripts (Novogene). In this step, clean data (clean reads) were obtained by removing reads containing adapter, reads containing ploy-N or low quality reads (> 50% of bases have a Qphred <= 20) from raw data. At the same time, Q20, Q30 and GC content the clean data were calculated. All the downstream analyses were based on the clean data with high quality. Index of the reference genome was built using HISAT2 v2.0.5 and paired-end clean reads were aligned to the reference genome (mus_musculus_Ensembl_97) using HISAT2 v2.0.5 (Kim et al., 2015). Read counts were quantified by featureCounts v1.5.0-p3 (Liao et al., 2014), normalized by TMM

(Trimmed Mean of M-values) method by edgeR (v3.30.3) (Robinson et al., 2010), and converted to Wagner's TPM (Transcripts per Million) (Wagner et al., 2012). Gene with TPM > 1 in at least 20% samples were considered as robustly expressed and kept for downstream analysis.

RNA sequencing of cDNA library from heart (for validation)

Raw data (raw reads) of fastq format were firstly processed through in-house perl scripts (Biomarker Technologies). In this step, clean data (clean reads in the range of 27.2-31.5 million) were obtained by removing reads containing adapter, reads containing ploy-N and low-quality reads from raw data. At the same time, Q20, Q30, GC-content and sequence duplication level of the clean data were calculated.The adaptor sequences and low-quality sequence reads were removed from the data sets. These clean reads were then mapped to the reference genome sequence. Only reads with a perfect match or one mismatch were further analyzed and annotated based on the reference genome (GRCm38/mm10). Hisat2 tools (v2.0.4) were used to map with reference genome. Read counts were quantified by StringTie (Pertea et al., 2015), normalized by TMM (Trimmed Mean of M-values) method by edgeR (v3.30.3) (Robinson et al., 2010), and converted to Wagner's TPM (Transcripts per Million) (Wagner et al., 2012). Gene with TPM > 1 in at least 20% samples were considered as robustly expressed and kept for downstream analysis.

RNA sequencing of cDNA library from kidney

The sequencing data was filtered via SOAPnuke (v1.5.2) by removing reads containing sequencing adapter, reads with a low-quality base ratio (base quality less than or equal to 5) of > 20%, reads with an unknown base ('N' base) ratio of > 5% (Li et al., 2008). Then, clean reads were obtained and stored in FASTQ format. The clean reads were mapped to the reference genome (GRCm38.p6) using HISAT2 (v2.0.4) (Kim et al., 2015). Bowtie2 (v2.2.5) was applied to align the clean reads to the reference coding gene set (Langmead and Salzberg, 2012). Read counts were quantified by RSEM (v1.2.12) (Li and Dewey, 2011), normalized by TMM (Trimmed Mean of M-values) method by edgeR (v3.30.3) (Robinson et al., 2010), and converted to Wagner's TPM (Transcripts per Million) (Wagner et al., 2012). Gene with TPM > 1 in at least 20% samples were considered as robustly expressed and kept for downstream analysis.

Bioinformatics for previous transcript profiling datasets

Data normalization were performed as follows. Microarray intensity files from GSE52333 and GSE87425 were log2 transformed, subtracted by the median of the sample, and universally added to one median (6.514206 and 6.801615, respectively). Microarray intensity data from GSE93903, expressed in log2 values, was subtracted by the median of the sample, and universally added to one median, 5.107950. RNA-seq data from GSE107787, expressed in RPKM, was used for downstream analysis.

Bioinformatics for untargeted metabolomics

Intensity data per group (treatment ~ time point) were checked for Pearson's correlation. The threshold is r >= 0.8 for at least 4 samples per group. In heart samples, N00_2, N04_5,

N08_1, D00_1, and D20_4 were removed. In liver samples, D00_3 and D04_2 were removed. Only one missing value was spotted, i.e. “5-Hydroxyhexanoic acid” in N16_1 in liver, which was replaced by the minimum in that group (N16). Processed data were subjected to circadian rhythmicity analysis as follows.

Bioinformatics for targeted lipidomics

Quantification data per group (treatment ~ time point) were checked for Pearson’s correlation. All samples exhibited a r > 0.99 per group, except DRF04_4 in adipose lipidomics study. DRF04_4 was excluded for downstream analysis for its dramatic deviation from the rest of the samples in DRF04. Data were subjected to circadian rhythmicity analysis as below.

Circadian Rhythmicity Analysis

By incorporating results from JTK_Cycle (JTK) and Lomb-Scargle (LS) methods, the MetaCycle::meta2d function was applied to determine circadian rhythmicity of normalized gene/metabolite/circRNA data from global profiling of transcripts, metabolites or lipids (Wu et al., 2016). meta2d p-value was imputed to Fisher’s method, and q-value was imputed to Benjamini-Hochberg (BH) multiple testing procedure. Data were not duplicated nor concatenated. The period length under light/dark cycles is set to 24 h. The period length under constant light is set to 20-28h. To capture 12h rhythms, the period length is set to 12 h (transcripts) and 8-28 h (lipids). BH.Q-value < 0.05 is considered as statistical significance for all genes, except lipids, and metabolites (meta2d_p-value < 0.01) and genes from validation studies of heart (meta2d_pvalue < 0.1, the relaxed p-value was meant to acquire more oscillating genes to capture the general pattern).

Rhythmicity analysis for lncRNA transcript dataset was performed as follows. Quantification profile of lncRNAs was subsetted from the transcriptome profile, and subjected to meta2d function. FDR (meta2d_BH.Q) < 0.05 is considered as statistical significance.

Comparison of circadian rhythm parameters (i.e. mesor, amplitude, phase) between two oscillating groups was computed by circaCompare (Parsons et al., 2020). When circaCompare could not be applied, such as period lengths of the two groups are different or at least one group is not oscillating, circadian rhythm parameters were computed by MetaCycle (Wu et al., 2016).

Phase Set Enrichment Analysis

Phase set enrichment analysis (Zhang et al., 2016) was performed on oscillating genes in different tissues to identify phase-clustered pathways from Gene Ontology gene sets (Source files: c5.all.v7.1.symbols.gmt, c5.bp.v7.1.symbols.gmt, c5.cc.v7.1.symbols.gmt, c5.mf.v7.1.symbols.gmt), which are curated in the Molecular Signatures Database (Broad Institute, MA, USA). Mouse gene nomenclature was converted to human gene nomenclature via “Human and Mouse Homology Classes with Sequence information” (curated by http://www.informatics.jax.org). Domain was set from 0 to 24, indicating the minimal and maximal period length is 0 and 24 h, respectively. Minimal and maximal items per set are 10 and 10000, respectively. Q-value < 0.05 is considered as statistical significance.

Cistrome Enrichment Analysis

Chromosomal location of genes was probed for what factors have a significant binding overlap with your peak set and submitted to http://dbtoolkit.cistrome.org/. Species: Mouse mm10. Data type in Cistrome: Transcription factor, chromatin regulator. Peak number of Cistrome sample to use: Top 1k peaks according to peak enrichment. Chromosomal location of genes covered each gene's 10,000 bp region upstream the transcription-start-site and the gene body.

Visualization

Heatmap of expression profile was visualized by R package: pheatmap with row-wise scaling and gene-specific clustering by Euclidean correlation. Sequencing reads of genes and lncRNAs were visualized on Integrative Genomics Viewer (Broad Institute, Boston, MA). Statistical analysis were imputed and visualized via R packages ggpubr or ggplot2, or via Prism 8.0.1 (RT-qPCR).

To determine the logical relations of oscillating gene/metabolite sets between NRF and DRF, VennDiagram analysis was performed (Chen and Boutros, 2011). The intersected group represents gene/metabolites that oscillated in tissues on both NRF and DRF, whose phase was examined. The groups unique to either NRF or DRF represent genes that oscillate exclusively on one restricted feeding regimen. To determine the logical relations of oscillating gene sets identified in different dietary regimens, UpSetR plot was applied to gene sets (R package: UpSetR 1.4.0).

Statistics

Sample size was determined by Guidelines for Genome-Scale Analysis of Biological Rhythms (Hughes et al., 2017). Principal components analysis was conducted with processed omics data by dudi.pca function in R package: ade4, with the number of axes set to 10. Q-value (FDR) < 0.05, p-value < 0.01 (for lipids, and metabolites) or p-value < 0.1 (for validation study of cardiac transcriptome, n = 1 per time point) is considered as reaching statistical significance. Multiple t-tests with Bonferroni correction were performed in R or Prism 8.0.1 (RT-qPCR) as indicated, and $P < 0.05$ is considered as statistical significance.

ADDITIONAL RESOURCES

KEY RESOURCES TABLE

KEY RESOURCES TABLE

REAGENT or RESOURCE	SOURCE	IDENTIFIER
Critical Commercial Assays		
Eastep® Super Total RNA Extraction Kit	Promega	Cat# LS1040
GoScript™ Reverse Transcription Mix	Promega	Cat# A2801
iTaq™ universal SYBR ® Green Supermix	Bio-Rad	Cat# 1725124
Deposited Data		
Raw and analyzed data (RNA-seq)	This paper	GEO: GSE150385
Analyzed data (RNA-seq, metabolomics, lipidomics, code)	This paper	Mendeley Data DOI: 10.17632/mb25x9t4m7.1
Transcriptomics, heart	This paper	CNGBdb：CNP0001640
Transcriptomics, visceral adipose tissue	This paper	CNGBdb：CNP0001638
Transcriptomics, kidney	This paper	CNGBdb：CNP0001605
Transcriptomics, liver	This paper	CNGBdb：CNP0001639
Experimental Models: Cell Lines		
Experimental Models: Organisms/Strains		
Mus musculus, C57BL/6J, male, 6 weeks, special pathogen-free	Hunan SJA Laboratory Animal Co. LTD	http://www.hnsja.com/product/7.html
Mus musculus, C57BL/6J, female, 6-7 weeks, special pathogen-free	Hunan SJA Laboratory Animal Co. LTD	http://www.hnsja.com/product/7.html

Chemicals, Peptides, and Recombinant Proteins		
Chloroform (HPLC grade)	Honeywell	Cat#049-4
Methanol (HPLC grade)	Fisher chemical	Cat#A452-4
Acetonitrile (LCMS grade)	Fisher chemical	Cat#A955-4
Ammonium hydroxide solution	Sigma-Aldrich	Cat#05002-1L
Ammonium acetate	Sigma-Aldrich	Cat#73594
Formic acid (98%)	J&K	Cat#299272
RIPA lysis buffer	Meilunbio	Cat#MA0151
Protease inhibitor cocktail	Sigma-Aldrich	Cat#P8340-5ML
d5-DAG(1,3-17:0)	Avanti Polar Lipids	Cat#110537
d5-DAG(1,3-18:1)	Avanti Polar Lipids	Cat#110581
19:0-CoA	Avanti Polar Lipids	Cat#870738
TAG(14:0)3-d5	CDN Isotopes	Cat#D-6958
TAG(16:0)3-d5	CDN Isotopes	Cat#D-5815
TAG(18:0)3-d5	CDN Isotopes	Cat#D-5816
Cholesterol-26,26,26,27,27,27-d6	CDN Isotopes	Cat#D-2139
Cholesteryl-2,2,3,4,4,6-d6 Octadecanoate	CDN Isotopes	Cat#D-5823
L-Phenylalanine-d8	Cambridge Isotope Laboratories	Cat# DLM-372-1
L-Tryptophan-d8	Cambridge Isotope Laboratories	Cat#DLM-6903-0.25

L-Isoleucine-d10	Cambridge Isotope Laboratories	Cat#DLM-141-0.1
L-Asparagine-13C4	Cambridge Isotope Laboratories	Cat#CLM-8699-H-0.05
L-Methionine-d3	Cambridge Isotope Laboratories	Cat#DLM-431-1
L-Valine-d8	Cambridge Isotope Laboratories	Cat#DLM-311-0.5
L-Proline-d7	Cambridge Isotope Laboratories	Cat#DLM-487-0.1
L-Alanine-d7	Cambridge Isotope Laboratories	Cat#DLM-251-PK
DL-Serine-d3	Cambridge Isotope Laboratories	Cat#DLM-1073-1
L-Phenylalanine-d8	Cambridge Isotope Laboratories	Cat# DLM-372-1
L-Tryptophan-d8	Cambridge Isotope Laboratories	Cat#DLM-6903-0.25
L-Isoleucine-d10	Cambridge Isotope Laboratories	Cat#DLM-141-0.1

L-Asparagine-13C4	Cambridge Isotope Laboratories	Cat#CLM-8699-H-0.05
L-Methionine-d3	Cambridge Isotope Laboratories	Cat#DLM-431-1
L-Valine-d8	Cambridge Isotope Laboratories	Cat#DLM-311-0.5
L-Proline-d7	Cambridge Isotope Laboratories	Cat#DLM-487-0.1
L-Alanine-d7	Cambridge Isotope Laboratories	Cat#DLM-251-PK
DL-Glutamic acid-d5	Cambridge Isotope Laboratories	Cat#DLM-357-0.25
L-Aspartic acid-d3	Cambridge Isotope Laboratories	Cat#DLM-546-0.1
L-Arginine-d7	Cambridge Isotope Laboratories	Cat#DLM-541-0.1
L-Glutamine-d5	Cambridge Isotope Laboratories	Cat#DLM-1826-0.1
L-Lysine-d9	Cambridge Isotope Laboratories	Cat#DLM-570-0.1

L-Histidine-d5	Cambridge Isotope Laboratories	Cat#DLM-7855
Taurine-13C 2	Cambridge Isotope Laboratories	Cat#CLM-6622-0.25
Betaine-d11	Cambridge Isotope Laboratories	Cat#DLM-407-1
Urea-(13C,15N2)	Cambridge Isotope Laboratories	Cat#CLM-234-0.5
L-lactate-13C3	Sigma-Aldrich	Cat#485926-500MG
Trimethylamine N-oxide-d9	Cambridge Isotope Laboratories	Cat#DLM-4779-1
Choline-d10	Cambridge Isotope Laboratories	Cat#DLM-141-0.1
Malic acid-d3	Cambridge Isotope Laboratories	Cat#DLM-9045-0.1
Citric acid-d4	Cambridge Isotope Laboratories	Cat#DLM-3487-0.5
Succinic acid-d4	Cambridge Isotope Laboratories	Cat#DLM-584-1
Fumaric acid-d4	Cambridge Isotope Laboratories	Cat#DLM-7654-1

Hypoxanthine-d3	Cambridge Isotope Laboratories	Cat#DLM-2923-0.1
Xanthine-15N2	Cambridge Isotope Laboratories	Cat#NLM-1698-0.1
Thymidine (13C10,15N2)	Cambridge Isotope Laboratories	Cat#CNLM-3902-25
Inosine-15N4	Cambridge Isotope Laboratories	Cat#NLM-4264-0.01
Cytidine-13C5	Cambridge Isotope Laboratories	Cat#CLM-3679-0.05
Uridine-d2	Cambridge Isotope Laboratories	Cat#DLM-7693-0.05
Methylsuccinic acid-d6	Cambridge Isotope Laboratories	Cat#DLM-2960-1
Benzoic acid-d5	Cambridge Isotope Laboratories	Cat#DLM-122-1
Creatine-d3	Cambridge Isotope Laboratories	Cat#DLM-1302-0.25
Creatinine-d3	Cambridge Isotope Laboratories	Cat#DLM-3653-0.1

Glutaric acid-d4	Cambridge Isotope Laboratories	Cat#DLM-3106-5
Glycine-d	Cambridge Isotope Laboratories	Cat# DLM-1674-5
Kynurenic acid-d5	Cambridge Isotope Laboratories	Cat#DLM-7374-PK
L-Citrulline-d4	Cambridge Isotope Laboratories	Cat#DLM-6039-0.01
L-Threonine-(13C4,15N)	Cambridge Isotope Laboratories	Cat#CNLM-587-0.1
L-Tyrosine-d7	Cambridge Isotope Laboratories	Cat#DLM-589-0.05
P-cresol sulfate-d7	Cambridge Isotope Laboratories	Cat#DLM-9786-0.01
Sarcosine-d3	Cambridge Isotope Laboratories	Cat#DLM-6874-0.1
Trans-4-hydroxy-L-proline-d3	Cambridge Isotope Laboratories	Cat#DLM-9778-PK
Uric acid-(13C; 15N3)	Cambridge Isotope Laboratories	Cat#CNLM-10617-0.001
Software and Algorithms		

R Project for Statistical Computing	https://www.r-project.org	V4.0.2 RRID:SCR_001905
RStudio	http://www.rstudio.com	v1.2.5033
R package: edgeR	(Robinson et al. 2010)	v3.30.3
R package: MetaCycle	(Wu et al., 2016)	v1.2.0 https://github.com/gangwug/MetaCycle
R package: circacompare	(Parsons et al., 2020)	v0.1.0
R package: ade4	(Dray and Dufour, 2007)	v1.7-16
R package: ggpubr	https://www.rdocumentation.org/packages/ggpubr	v0.2.5
R package: ggplot2	https://cran.r-project.org/web/packages/ggplot2/index.html	RRID:SCR_014601
R package: dplyr	https://cran.r-project.org/web/packages/dplyr/index.html	RRID:SCR_016708
R package: VennDiagram	(Chen and Boutros, 2011)	v1.6.20 https://cran.r-project.org/web/packages/VennDiagram/index.html

R package: pheatmap	https://cran.r-project.org/web/packages/pheatmap/index.html	v1.0.12
R package: UpSetR	https://cran.r-project.org/web/packages/UpSetR/	v1.4.0
HISAT2	(Kim et al., 2015)	http://ccb.jhu.edu/software/hisat2
StringTie	(Pertea et al., 2015)	https://ccb.jhu.edu/software/stringtie/
featureCount	(Liao et al., 2014)	1.5.0-p3 http://subread.sourceforge.net/
Cufflinks	(Trapnell et al., 2012)	http://cole-trapnell-lab.github.io/cufflinks/
find_circ	(Memczak et al., 2013)	https://github.com/marvin-jens/find_circ
rMATS	(Shen et al., 2014)	http://rnaseq-mats.sourceforge.net/index.html
CIRI	(Gao et al., 2015)	https://sourceforge.net/projects/ciri/
Phase Set Enrichment Analysis	(Zhang et al., 2016)	https://github.com/ranafi/PSEA
Integrative Genomics Viewer (IGV)	http://software.broadinstitute.org/software/igv/home	v2.8.0

Mendeley Desktop	https://www.mendeley.com/?interaction_required=true	v1.19.4
Excel 2019	Microsoft	N/A
Graphpad Prism 8.0.1	https://www.graphpad.com	v8.0.1
Other		
Normal chow diet (Rodent maintenance diet)	Hunan SJA Laboratory Animal Co. LTD	http://www.hnsja.com/product/13.html

Supplemental References

Chen, H., Boutros, P.C., 2011. VennDiagram: a package for the generation of highly-customizable Venn and Euler diagrams in R. BMC Bioinformatics 12, 35. https://doi.org/10.1186/1471-2105-12-35

Chen, R., Seo, D.O., Bell, E., Von Gall, C., Lee, D.C., 2008. Strong resetting of the mammalian clock by constant light followed by constant darkness. J. Neurosci. 28, 11839–11847. https://doi.org/10.1523/JNEUROSCI.2191-08.2008

Dray, S., Dufour, A.-B., 2007. The ade4 Package: Implementing the Duality Diagram for Ecologists. J. Stat. Softw. 22. https://doi.org/10.18637/jss.v022.i04

Gao, Y., Wang, J., Zhao, F., 2015. CIRI: An efficient and unbiased algorithm for de novo circular RNA identification. Genome Biol. 16, 1–16. https://doi.org/10.1186/s13059-014-0571-3

Kim, D., Langmead, B., Salzberg, S.L., 2015. HISAT: a fast spliced aligner with low memory requirements. Nat. Methods 12, 357–360. https://doi.org/10.1038/nmeth.3317

Lam, S.M., Zhou, T., Li, J., Zhang, S., Chua, G.H., Li, B., Shui, G., 2020. A robust, integrated platform for comprehensive analyses of acyl-coenzyme As and acyl-carnitines revealed chain length-dependent disparity in fatty acyl metabolic fates across Drosophila development. Sci. Bull. 65, 1840–1848. https://doi.org/10.1016/j.scib.2020.07.023

Langmead, B., Salzberg, S.L., 2012. Fast gapped-read alignment with Bowtie 2. Nat. Methods 9, 357–359. https://doi.org/10.1038/nmeth.1923

Li, B., Dewey, C.N., 2011. RSEM: accurate transcript quantification from RNA-Seq data with or without a reference genome. BMC Bioinformatics 12, 323. https://doi.org/10.1186/1471-2105-12-323

Li, R., Li, Y., Kristiansen, K., Wang, J., 2008. SOAP: short oligonucleotide alignment program. Bioinformatics 24, 713–714. https://doi.org/10.1093/bioinformatics/btn025

Liao, Y., Smyth, G.K., Shi, W., 2014. featureCounts: an efficient general purpose program for

assigning sequence reads to genomic features. Bioinformatics 30, 923–930. https://doi.org/10.1093/bioinformatics/btt656

Lu, J., Lam, S.M., Wan, Q., Shi, L., Huo, Y., Chen, L., Tang, X., Li, B., Wu, X., Peng, K., Li, M., Wang, S., Xu, Y., Xu, M., Bi, Y., Ning, G., Shui, G., Wang, W., 2019. High-Coverage Targeted Lipidomics Reveals Novel Serum Lipid Predictors and Lipid Pathway Dysregulation Antecedent to Type 2 Diabetes Onset in Normoglycemic Chinese Adults. Diabetes Care 42, 2117–2126. https://doi.org/10.2337/dc19-0100

Memczak, S., Jens, M., Elefsinioti, A., Torti, F., Krueger, J., Rybak, A., Maier, L., Mackowiak, S.D., Gregersen, L.H., Munschauer, M., Loewer, A., Ziebold, U., Landthaler, M., Kocks, C., Le Noble, F., Rajewsky, N., 2013. Circular RNAs are a large class of animal RNAs with regulatory potency. Nature 495, 333–338. https://doi.org/10.1038/nature11928

Parkhomchuk, D., Borodina, T., Amstislavskiy, V., Banaru, M., Hallen, L., Krobitsch, S., Lehrach, H., Soldatov, A., 2009. Transcriptome analysis by strand-specific sequencing of complementary DNA. Nucleic Acids Res. 37, e123–e123. https://doi.org/10.1093/nar/gkp596

Parsons, Rex, Parsons, Richard, Garner, N., Oster, H., Rawashdeh, O., 2020. CircaCompare: A method to estimate and statistically support differences in mesor, amplitude and phase, between circadian rhythms. Bioinformatics 36, 1208–1212. https://doi.org/10.1093/bioinformatics/btz730

Pertea, M., Pertea, G.M., Antonescu, C.M., Chang, T.C., Mendell, J.T., Salzberg, S.L., 2015. StringTie enables improved reconstruction of a transcriptome from RNA-seq reads. Nat. Biotechnol. 33, 290–295. https://doi.org/10.1038/nbt.3122

Robinson, M.D., McCarthy, D.J., Smyth, G.K., 2010. edgeR: a Bioconductor package for differential expression analysis of digital gene expression data. Bioinformatics 26, 139–140. https://doi.org/10.1093/bioinformatics/btp616

Shen, S., Park, J.W., Lu, Z.X., Lin, L., Henry, M.D., Wu, Y.N., Zhou, Q., Xing, Y., 2014. rMATS: Robust and flexible detection of differential alternative splicing from replicate RNA-Seq data. Proc. Natl. Acad. Sci. U. S. A. https://doi.org/10.1073/pnas.1419161111

Song, J.W., Lam, S.M., Fan, X., Cao, W.J., Wang, S.Y., Tian, H., Chua, G.H., Zhang, C., Meng, F.P., Xu, Z., Fu, J.L., Huang, L., Xia, P., Yang, T., Zhang, S., Li, B., Jiang, T.J., Wang, R., Wang, Z., Shi, M., Zhang, J.Y., Wang, F.S., Shui, G., 2020. Omics-Driven Systems Interrogation of Metabolic Dysregulation in COVID-19 Pathogenesis. Cell Metab. 32, 188-202.e5. https://doi.org/10.1016/j.cmet.2020.06.016

Trapnell, C., Roberts, A., Goff, L., Pertea, G., Kim, D., Kelley, D.R., Pimentel, H., Salzberg, S.L., Rinn, J.L., Pachter, L., 2012. Differential gene and transcript expression analysis of RNA-seq experiments with TopHat and Cufflinks. Nat. Protoc. 7, 562–578. https://doi.org/10.1038/nprot.2012.016

Wagner, G.P., Kin, K., Lynch, V.J., 2012. Measurement of mRNA abundance using RNA-seq data: RPKM measure is inconsistent among samples. Theory Biosci. 131, 281–285. https://doi.org/10.1007/s12064-012-0162-3

Woldegiorgis, G., Spennetta, T., Corkey, B.E., Williamson, J.R., Shrago, E., 1985. Extraction of tissue long-chain acyl-CoA esters and measurement by reverse-phase high-performance liquid chromatography. Anal. Biochem. 150, 8–12. https://doi.org/10.1016/0003-2697(85)90434-8

Wu, G., Anafi, R.C., Hughes, M.E., Kornacker, K., Hogenesch, J.B., 2016. MetaCycle: An integrated R package to evaluate periodicity in large scale data. Bioinformatics 32, 3351–3353. https://doi.org/10.1093/bioinformatics/btw405

Yuan, M., Breitkopf, S.B., Yang, X., Asara, J.M., 2012. A positive/negative ion-switching, targeted mass spectrometry-based metabolomics platform for bodily fluids, cells, and fresh and fixed tissue. Nat. Protoc. 7, 872–881. https://doi.org/10.1038/nprot.2012.024

Zhang, R., Podtelezhnikov, A.A., Hogenesch, J.B., Anafi, R.C., 2016. Discovering Biology in Periodic Data through Phase Set Enrichment Analysis (PSEA). J. Biol. Rhythms 31, 244–257. https://doi.org/10.1177/0748730416631895